

Chapter 6

The Beauregard massive deep-seated landslide

6.1 Introduction

The Beauregard Landslide is a deep-seated gravitational slope deformation in a rock mass comprised of gneiss and micaschist, with prasinite intercalations. Due to the presence at the toe of an important arch gravity dam, built in the fifties, the landslide has been widely studied. A monitoring system of both the left slope and the dam has been operative since the first infilling of the reservoir and subsequently updated with state of the art systems. The instability phenomena have been studied in detail in recent years as described in a number of papers and reports (Barla et al. (2005, 2006, 2007, 2008a,b, 2009a,b, 2010a,b, 2011); Barla and Chiappone (2006); Barla (2009, 2010); Miller et al. (2008); Kalenchuk et al. (2010); Martinotti (2010)).

This landslide and some of the instability modes which characterise it are taken as a case study for the present thesis. With the intent to provide an appropriate reference for the studies described in the following, this chapter is intended to give first a short description of the geological and geomechanical conditions of the landslide, in conjunction with the monitoring data analysis and interpretation undertaken, which allow one to explain some of its major behavioural features. Then, the failure mechanisms to be analysed with the combined discrete-finite element approach described and validated in the previous chapters will be described.

Dam Authority has declared in 2004 that “the dam should be dismissed unless effective means are found to slow down the slope movement” (Barla, 2010).

6.3 Geological setting

The rock mass foundation of the Beauregard dam is comprised of gneiss and micaschist belonging to the Gran San Bernardo Series, with prasinite intercalations. The two slopes of the Valgrisenche valley, where the dam is located, have different characteristics. On the right slope the rock mass is of good to excellent quality, on the left slope it is highly fractured, cataclastic, and mylonitic.

Since the beginning of fifties, following up the first geologic and geomorphologic studies for the Beauregard dam construction, on the N-W flank of the valley, a zone which could be interpreted as a potential large size landslide was recognized. During the dam construction phases, as reported by Desio (1973), a deep pocket of glacio-fluvial sediments was found on the left dam abutment excavation (Figure 6.2).

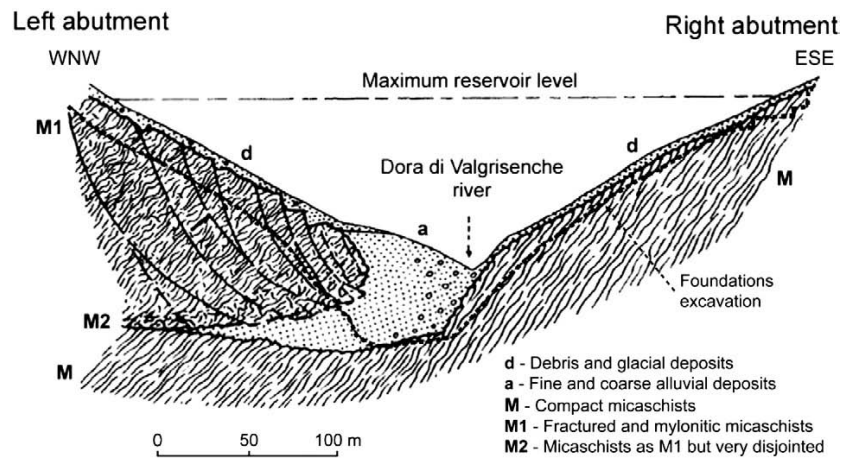


Figure 6.2: Geological cross section at the Beauregard dam site (from Desio 1973, modified).

The presence of these loose sediments posed very serious problems during construction of the dam and was of great concern for both water flow control and dam stability. The pocket of glacio-fluvial sediments was subsequently replaced by concrete to a depth

of 200 m into the left slope. In order to ensure water tightness a main grout curtain was constructed all around the dam to about 100 m below the Dora river bed.

The presence of large rock slices of the gneissic rocks of the Ruitor Unit directly overlying the glaciofluvial deposits is a clear evidence that after the last glacial Holocene debuttressing, the left slope toe has slipped down. In the last years, the whole left slope above the dam has been recognized and classified as a DSGSD (Barla et al., 2010a).

6.3.1 Geological model

Figure 6.3 illustrates the geological and morpho-structural map of the Valgrisenche left slope based on the studies carried out so far. Considering the geomorphologic features, the deformation zone involves a significant portion of the slope and extends approximately 1500 m in height from the toe (1700 m a.s.l.) to the mountain ridge (3200 m a.s.l.).

Steeply dipping into the slope are predominant sub-vertical (70° - 80°) discontinuities which strike parallel to the valley axis (NE-SW and NNE-SSW), associated to minor shear zones and discontinuities which are nearly orthogonal to them (ESE-WNW). The main schistosity planes along the Beauregard slope dip 25° to 30° to S and SW.

A main head scarp trending E-W with a maximum relief of about 250 m, associated with the double ridge of Becca de L'Aouille Mt., is evident in the north sector of the landslide and it is interpreted as the day-lighted weathered portion of the main scarp delimiting the DSGSD surface of rupture.

By Scavarda Refuge the scarp turns to the south forming a wide niche from which a rocky ridge (Scavarda ridge) has been lowered. The sector is highly weathered and fractured and it is affected by rock falls and toppling failures which result in discharge of rock in two main talus at the foot of the cliff, between 2100 and 2300 m a.s.l. In the upper part of the ridge, above the head scarp, a swarm of trenches up to 3 m wide trending parallel to the valley, is present. These trenches are the continuation towards SW of an alignment of scarps, counter-scarps and predominant joints cropping out between the Moriond Glacier and Becca de L'Aouille zone.

In the central portion of the landslide two distinct ridges are shown to the N (Bois De Goulaz) and to the S (Bochat) characterized by bulging and convex profile. Swarms of trenches up to several meters wide and oriented NE-SW, are developed behind both ridges. In the Alpettaz area, between 2000 and 2200 m a.s.l., one major concave scarp is present. It can be assumed to be the morphological expression of the basal sector of the landslide, moving towards the reservoir. At lower elevations (1800-2000 m a.s.l.), close to the reservoir, numerous minor linear scarps and counter-scarps, trending parallel to the valley axis, can be recognized.

Based on aerial photographs and detailed field work, the project area, including the

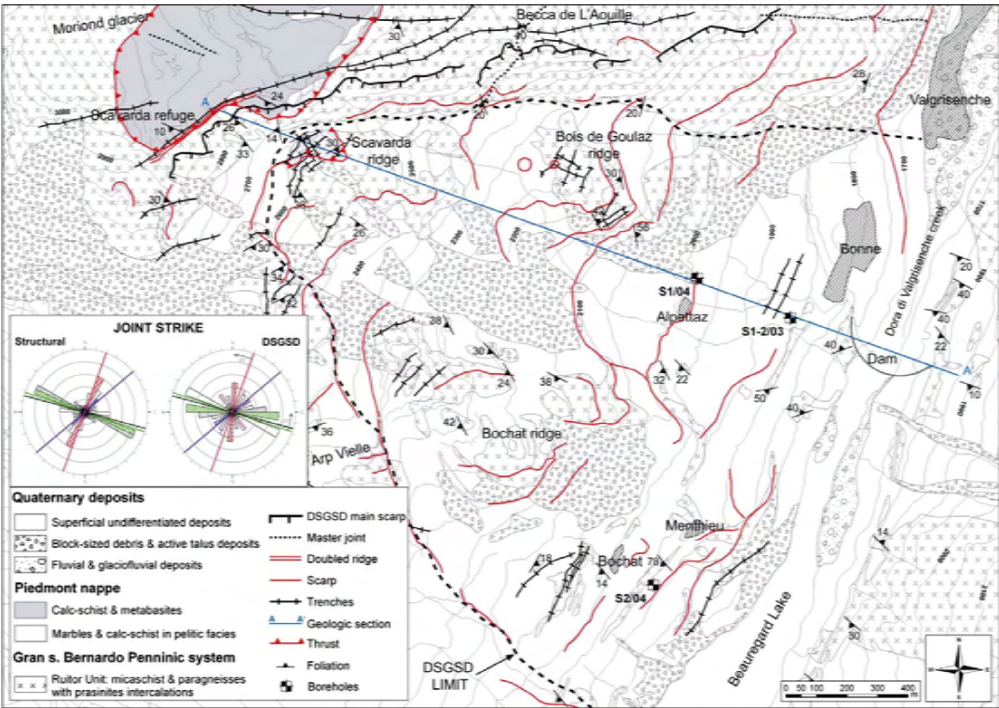


Figure 6.3: Geological and morpho-structural map of the Beaugard DSGSD. Rose diagrams show orientations of structural lineaments and the mean planes of the main discontinuity sets (Barla et al., 2010a).

right slope, could be subdivided into three zones which are characterised by different geomorphologic and geostructural features, different landslide mechanics as well as different landslide activity, as shown in Figure 6.4.

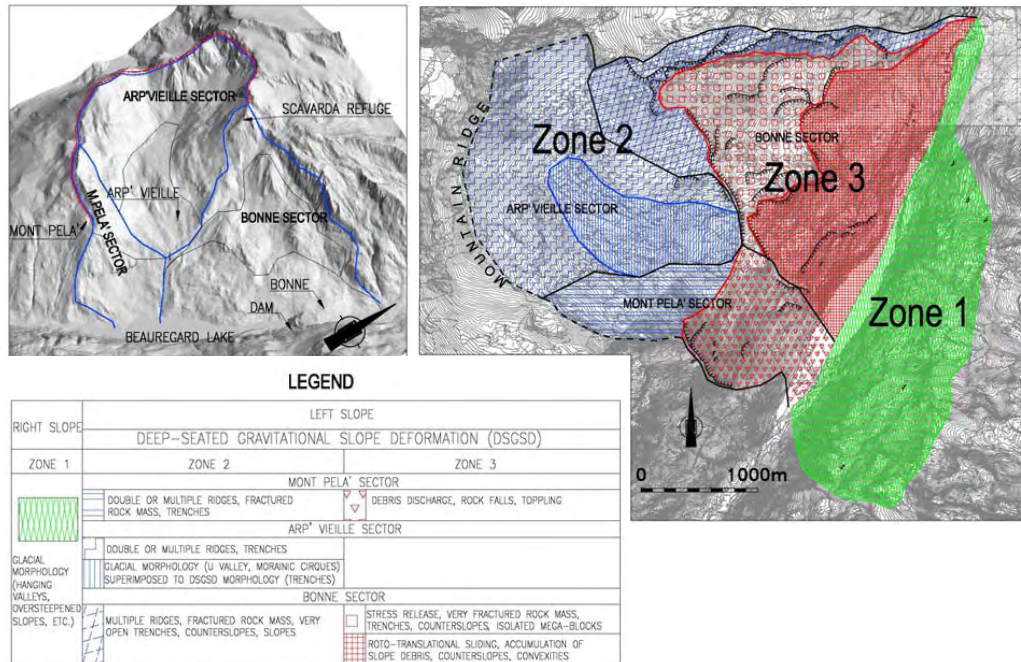


Figure 6.4: Map showing the investigated area and three zones characterised by different geomorphological features (Barla et al., 2006).

Zone 1, which comprises the right slope of the Valgrisenche valley, is characterised by typical glacial morphology which is underlined by the presence of hanging valleys, over-steepened slopes, and typical features owing to glacial erosion.

Zone 2, which develops in the upper part of the left slope, is bordered by the mountain ridge and the main head scarp of the active slope movement. It is characterised by the presence of a fractured rock mass, where double or multiple ridges, trenches, and accumulation of slope debris can be noted. The DSGSD in this zone is considered to be in an intermediate stage of development and in a stable condition.

Zone 3, which corresponds to the lower portion of the slope, is the active portion of

the DSGDS which, based on the monitoring data, is moving toward the reservoir.

6.4 Monitoring system

Monitoring of massive landslides is a common approach to hazard management. Installation of an extensive instrumentation system occurred from the time of the completion of the Beaugard Dam, including instruments installed both in the dam and in the left slope. Figure 6.5 gives the layout of the monitoring system for both the dam and the slope.

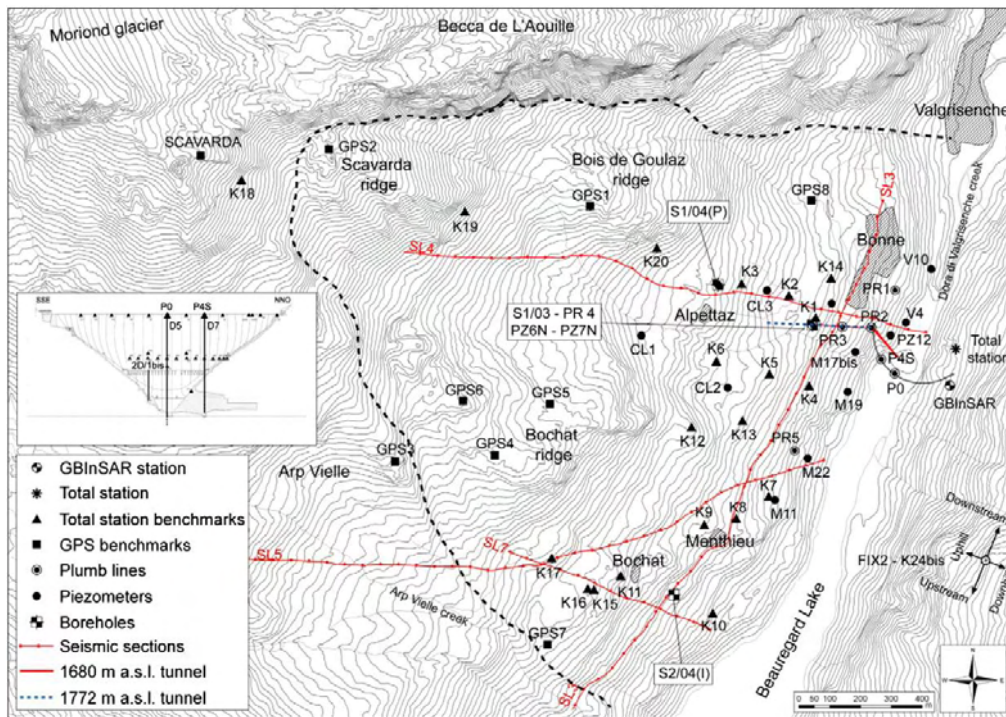


Figure 6.5: Monitoring system installed at the Beaugard site. The box on the left shows the position of the plumb lines (P0 and P4S), multipoint extensometer (2D/1bis) and total station benchmarks on the downstream face of the dam (Barla et al., 2010a).

The monitoring system installed along the landslide comprises both traditional and state of the art equipment. Traditional monitoring include piezometers, topographic benchmarks, most of them located within the landslide mass at the toe, and plumb lines on the left slope abutment. State of the art techniques comprise a total station Leica, GPS surveys, and more recently a ground based interferometric synthetic aperture radar (GBInSAR). Similarly, topographic benchmarks and two plumb lines are used for monitoring the dam response, in addition to the total station Leica.

6.4.1 Conventional monitoring results

Monitoring of the slope through the years has revealed that the rate of displacement is correlated to the water level in the reservoir and to the piezometric level in the slope. It has been observed that displacements occur during the spring (May-June) to late summer-early autumn (September-October) period, when snow melt takes place along the slope. Limited or no displacements are observed during the late autumn to late winter period.

The seasonal response of the slope may be outlined only by the plumb lines measurements. In Figure 6.6a the cumulated displacements measured at the head of PR3 and PR4 plumb lines are plotted together with the snow height.

It is clear that during the spring-summer time the rate of movement increases (see for example the displacements occurred from May to the end of August 2006). Such a movement is a consequence of snow melting and the raising of the piezometric level. This is well shown in Figure 6.6b where the piezometric level and the snow height are plotted. Following snow melting, the piezometers show a significant increase of piezometric level, up to 15-20 m, which appears to be well correlated with the displacement triggered in the slope. The raising of the groundwater level is dependent on the amount of snow cumulated during the winter period. This is true only for piezometers located at the toe of the slope, while for piezometers located at elevation greater than 2000 m a.s.l. (S1/04 and CL1) the increase of groundwater level is not influenced by the thickness of snow cover.

The slope movement recorded by the total station is cyclic. The results of statistical analysis of data recorded at four total station targets are shown in Figure 6.7. For each target considered, the reversible and irreversible effects are plotted together with the measured and predicted values. Considering that the uphill-downhill component is plotted, the irreversible displacement of the slope is about 14.2 mm for K1, 24.4 mm for K4, 14.4 mm for K13 and 33.5 mm for K19 in the downhill direction (Figure 6.7). The period taken into account is 6.5 years.

It is observed that by comparing the displacement rates measured on the same tar-

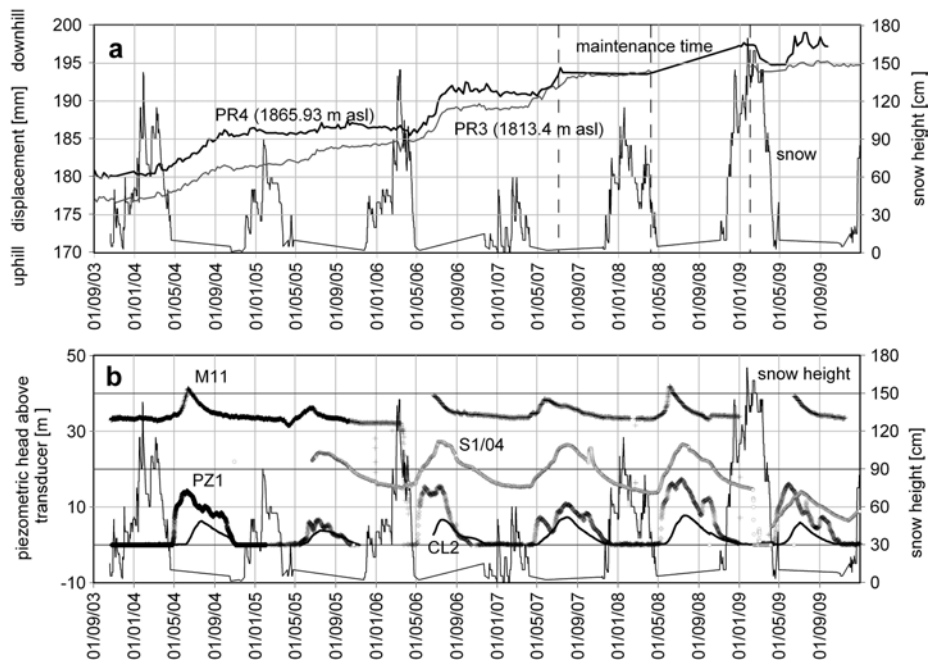


Figure 6.6: Slope cumulated displacements at the top of PR3 and PR4 plumb lines and snow height (a); snow height and water level in piezometers (CL2, M11, PZ1 and S1/04) (b) (Barla et al., 2010a).

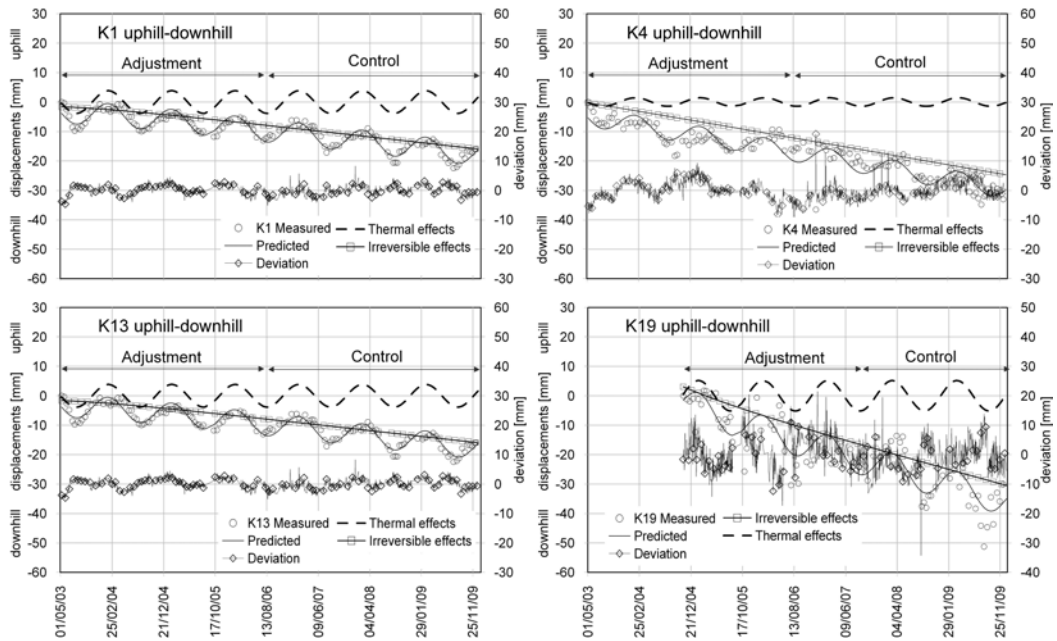


Figure 6.7: K1, K4, K13 and K19 total station targets installed on the slope: comparison between predicted and measured displacements based on statistical prediction model, thermal and irreversible components of displacements, standard deviation (Barla et al., 2010a).

gets by the automatic total station and manual topographic system, some differences arise between the two systems (Figure 6.8). The total station highlights the downslope displacement component while the manual topographic measurements indicate both a downslope and downstream component of the movement. Referring to the slope monitoring data, the average displacement rates of targets located in Bonne and Alpettaz areas are about 4-6 mm/year. In the Bochat area, 1 km upstream from the dam, the average displacement rate increases to 10-13 mm/year. The horizontal downslope displacement represents the most significant component of the slope movement and it is 5 times the vertical component.

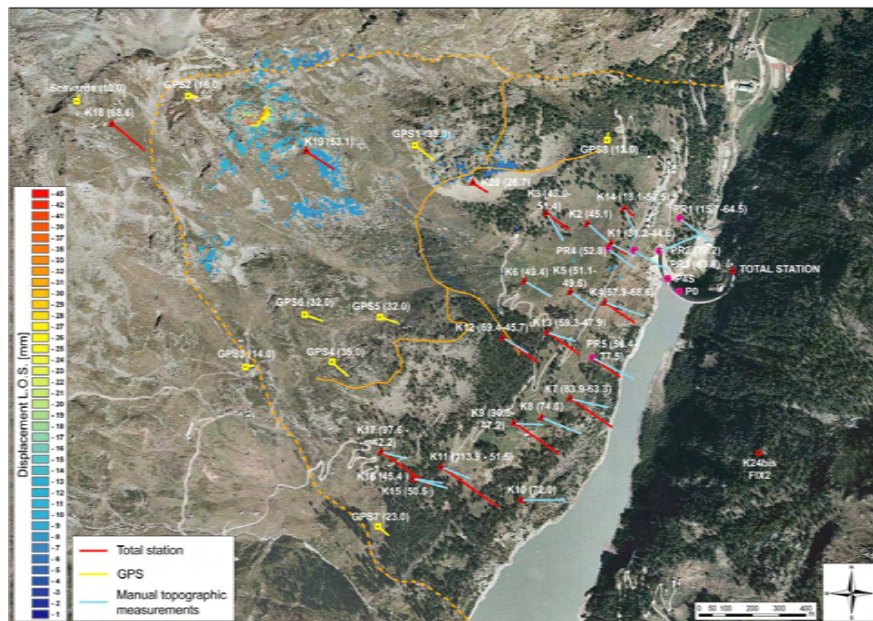


Figure 6.8: Map showing displacements vectors measured on the landslide monitoring network by GPS (August 2000-June 2007), total station (May 2003-June 2007), manual topographic system (May 2003-June 2007) and the results of the GBInSAR monitoring (June-October 2008). All the measures are expressed in mm (Barla et al., 2010a).

6.5 Key instabilities characterizing the massive landslide

The area affected by the DSGSD is characterised by a high degree of rock mass subdivision. The geometry of the discontinuities and the presence of a thick cataclastic zone at depth allow for the development of several instability mechanisms including sliding of large slope sectors on rotational or compound surfaces, rockfalls, block and flexural topples (Figure 6.9).

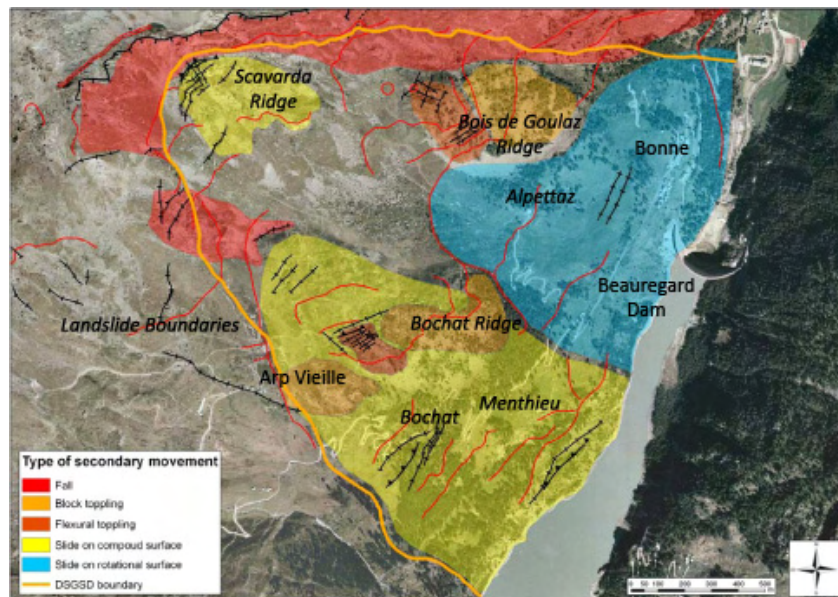


Figure 6.9: Key instabilities developed in Beauregard Landslide.

Series of minor scarps are present mostly in an area extending 1500 m upstream of the dam site. Predominant shears and joints are steeply dipping into and out of the slope. They strike parallel to the valley axis and are associated to minor shear and joints which are nearly orthogonal to them. Distinctive gravitational morpho-structures such as double and multiple ridges, trenches and open cracks, characteristic of deep-seated and large-scale massive landslides cover the whole area investigated.

Detailed site investigations of the slope (Alpettaz area) have allowed to identify a basal sliding zone delimiting the more active portion of the landslide. Essential in this interpretation have been the results of both seismic refraction and seismic reflection sur-

veys and boreholes drilling (S1/03 and S1/04). These boreholes have encountered a shear zone of maximum thickness 20 m, characterized by the presence of sheared cataclastic rock, locally reduced to soil like material with silt and clay (Barla et al., 2010a).

The Bochat-Arp Vieille area is characterized by sliding on a compound surface (yellow area in Figure 6.9). The seismic refraction surveys and most of all the results of borehole (S2/04 - Menthieu) drilling to a depth of 259.3 m show that the rock belonging to the shear zone is not yet reduced to soil like material. The major shear zone has been encountered at 147 m of depth, where the collected material changes from competent rock to sheared and crushed rock. The shear zone, 12 m thick, is interpreted as the continuation of the landslide basal shear surface towards the south-western sector of the slope.

Large flexural toppling failure mechanisms have been observed in the central portion of the landslide area (Bochat Ridge and Bois the Goulaz Ridge) where locally also block toppling occurs (Figure 6.9). The flexural toppling is mainly due to opening of tension cracks and trenches which strike parallel to the valley axis.

The upper portion of the landslide is highly weathered and fractured. The Scavarda Ridge is interpreted to be a large mass broken away from the headscarp. Morphostructures such as faults, open cracks and trenches, widespread along the Scavarda ridge, undergo a brittle deformation and interact with the basal portion of the landslide which exhibits a creep behaviour. Localized rockfall and toppling failures have developed talus accumulations below the headscarp.

6.6 Joint sets and main discontinuity features

The rock mass on the valley flank affected by the DSGSD is highly fractured, disjuncted and cataclastic. The geomechanical mapping carried out both on the surface and at depth during the excavation of the 1680 m a.s.l. left abutment tunnel, has shown the presence of 6 main joint sets (Figure 6.10). These are observed in the DSGSD area and their orientation is quite different from the orientation of the same joint sets observed along the left slope.

- K1 - joint set N-S trending, with sub-vertical dip (mean plane $100^{\circ}\pm 20^{\circ}/80^{\circ}\pm 15^{\circ}$);
- K2 - joint set E-W trending, with vertical dip (mean plane $185^{\circ}\pm 20^{\circ}/90^{\circ}\pm 10^{\circ}$); K1 and K2 are two conjugate sets;
- K3 - joint set E-W trending, with dip ranging from sub-horizontal to 50° (mean plane $360^{\circ}/30^{\circ}$);

- K4 - joint set NE-SW trending, parallel to the valley axis, sub-vertical dip (mean plane $140^{\circ}\pm 10^{\circ}/80^{\circ}\pm 10^{\circ}$);
- K5 - joint set NW-SW trending, orthogonal to the valley axis, with sub-vertical dip-angle (mean plane $55^{\circ}\pm 10^{\circ}/80^{\circ}\pm 10^{\circ}$); due to the quite variable spacing, K5 joint set is not very evident in several sectors of the landslide;
- K6 - joint set NW-SW trending, orthogonal to the valley axis, with mean dip of 35° (mean plane $55^{\circ}/30^{\circ}$).

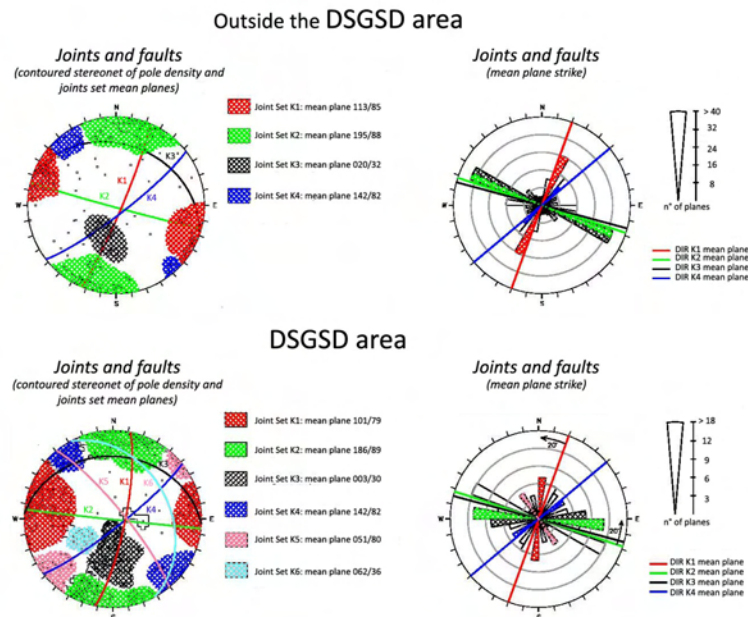


Figure 6.10: Stereograms and rose diagrams showing orientation of main discontinuity sets (Barla et al. 2010a, modified).

The persistence of K1, K2, K4 and K5 discontinuity sets can be estimated to be ranging from meters to tens of meters, whereas K3 and K6 persistence can be considered metric. Often the K3 and K6 discontinuities end along the schistosity planes and in some cases propagate as new fractures through the rock mass. This process can finally lead to the joining of adjacent discontinuities forming a “stepped surface”.

The spacing of the discontinuities, although not directly calculated using a statistical method, can be estimated by observing shape and size of rock blocks (superficial deposits). The maximum volume of blocks can reach 20-25 m³, but volumes of 0.25 m³ up to 5 m³ are much more common. The blocks have cubic or parallelepiped shape; columnar or slab shapes are occasionally present. The values of spacing, estimated from the observation of blocks volume and shape, are shown in Table 6.1.

Discontinuity Set	K1	K2	K3	K4	K5	K6
Spacing (m)	1-5	1-5	2-5	0.5-3	2-5	3-7

Table 6.1: Mean spacing of discontinuity sets.

The orientation of the schistosity planes has a great variability in the landslide area as shown in Figure 6.11. In the upper Valgrisenche valley, the schistosity dips towards S and SW with dip angles from 15° to 45° (mean plane 195°/30°). The dip direction has a marked variability due to successive folding phases which affected the Ruitor basement. The schistosity planes are pervasive inside micaschists and gneiss.

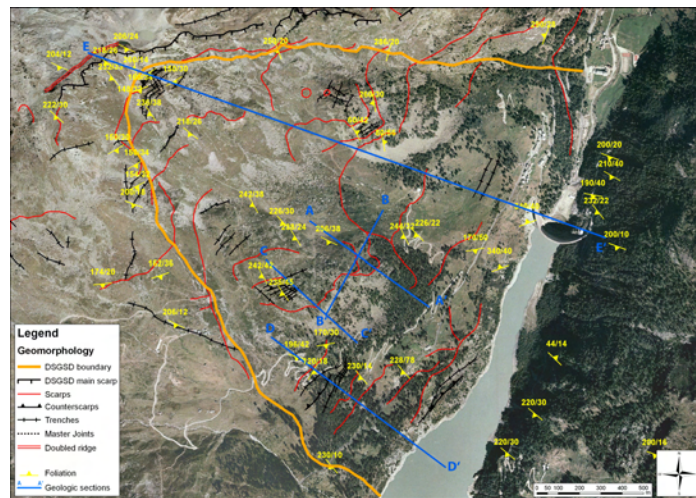


Figure 6.11: Map showing the cross sections: Bochat Ridge cross section A-A'; Bochat Ridge cross section B-B'; Arp Vieille cross section C-C'; Bochat D-D'; Bonne Alpetta Scavarda cross section E-E'. The orientation of the schistosity planes is also displayed.

6.6.1 Bochat ridge section (A-A'). Geological setting

The cross section A-A', with NW-SE trending, is located at the N-E termination of the Bochat ridge (Figure 6.11). The trend of the cross section is E36°S and its length is 685 m.

The orientations of the joint systems associated to the Bochat Ridge area are shown in Table 6.2. The section crosses orthogonally K4 and near orthogonally K1, whereas is parallel to K5. The orientation of the section with respect to the K2 mean plane is about 30°. The trace of the schistosity and K5 planes on the cross section is nearly horizontal.

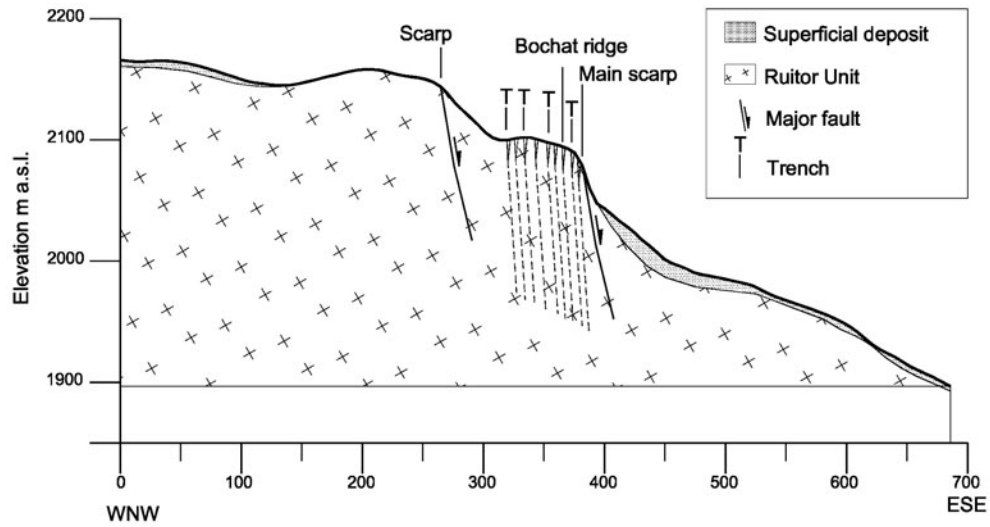
Joint Set	Dip Direction	Range of variation	Dip	range of variation
K1	100°	±20°	80°	±15°
K2	185°	±20°	90°	±10°
K3	000°	±15°	30°	±15°
K4	140°	±10°	80°	±15°
K5*	55°	±10°	80°	±10°
K6	55°	±5°	35°	±10°
Schistosity	195°	±30°	30°	±15°

* K5 joint set has a pluridecametric spacing.

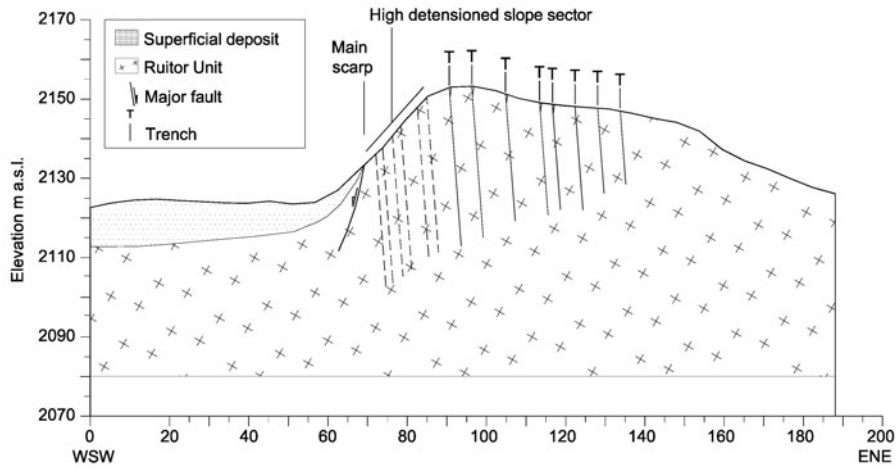
Table 6.2: Range of properties of joint sets on Bochat Ridge.

The interpreted geologic cross section is shown in Figure 6.12. Two main scarps which develop along the K4 joint set characterise the cross section. These scarps can be considered to be the morphological expressions of two sub-parallel normal faults and are characterized by a vertical displacement of 50 and 100 m respectively. At the toe of the lower scarp a thick talus is present. It is formed by the progressive accumulation of rock blocks mobilized along the rocky cliffs.

The instability mechanism observed is flexural toppling and locally block toppling. The rock columns are divided by widely spaced joints belonging to two orthogonal sub-vertical joint sets (K1+K4 and K2+K5). These columns bend forward and result in tensional breaking along the schistosity or K6 plane which dips out of the slope with a small angle. Sometimes the short columns placed at the slope toe are overloaded by the overturning longer columns which are above. It is common to observe columns thrusting forward which lead to further toppling of other columns. The flexural and block toppling is mainly forced by the freeze-thaw cycles of the water infiltrating along the structures. Repeated freeze-thaw cycles weaken the rock mass which, over time, breaks up along the joints into angular pieces. The angular rock fragments gather in the trenches and at the slope toe to form a talus.



(a)



(b)

Figure 6.12: Geological sections of Bochat Ridge: (a) A-A' geological section; (b) B-B' geological section.

6.6.2 Bochat ridge section (B-B'). Geological setting

The NE-SW trending cross section B-B' (Figure 6.11) is located towards the N-E termination of the Bochat ridge. The section, with length 190 m, has trend N29°E.

The joint set data, characteristic of the area, are shown in Table 6.2. The section B-B' crosses near-orthogonally K2 and K3 set, whereas it does not intersect the sub-vertical joint set K4, since its trend is parallel to the section. The section crosses a pronounced scarp, oriented E-W along the Bochat Ridge, related to the K2 system of faults recognized along the ridge (Figure 6.12).

Block toppling instability has been clearly observed. The columns of rock subjected to toppling are defined by two orthogonal sets of discontinuity (K1+K4 and K2+K5) with a spacing of 2-5 m. They partially slide along the schistosity planes dipping towards S-W (inclination 35°-40°) and partially break in tension along the K3 planes dipping towards N-E (inclination 25°-30°) and resulting in a stepped surface. All the frontal portion of the main scarp is characterized by a significant destressing of the rock mass. As the frontal rock columns collapse, the destressing and column sliding progressively move backward. Considering that block toppling is a 3D mechanism, also the K4 joint set has an important role in the development of this type of instability.

6.6.3 Arp Vieille section (C-C'). Geological setting

The geologic section C-C' (Figure 6.13), trending NW-SE, is located at the SW termination of the Bochat ridge. The length of the cross section is 570 m and its trend is E42°S. The joint set data which characterise this portion of the landslide are shown in Table 6.3. The section crosses orthogonally the K4 and near-orthogonally the K1 joint set (trending approximately N-S) which are characterized by wide openings (up to 5 m). The projection of the schistosity planes on the cross section is sub-horizontal, with a small inclination toward the slope. The pronounced scarp on the ridge edge can be considered to be the morphological expression of a normal fault developed along the K1 discontinuity set. On the top of the ridge, back-facing scarps and sinked sectors indicate the presence of a back-facing structure (fault). At the base of the scarp, a thick talus is present, formed by accumulation of the rock blocks mobilized along the cliff.

The failure mechanism developed along the frontal portion of the ridge is ascribed to flexural toppling. This type of instability occurs in rock with one preferred sub-vertical discontinuity system (K1-K4), nearly continuous. The rock columns or plates (which can be considered as cantilevers) bend forward resulting in tensional breaking along the schistosity or the K6 planes. The outward movement of each cantilever produces inter-layer sliding and back-facing scarps. In this way, the inclination of the sub-vertical discontinuity sets (K1-K4) progressively changes from valley (S-E direction), in the more

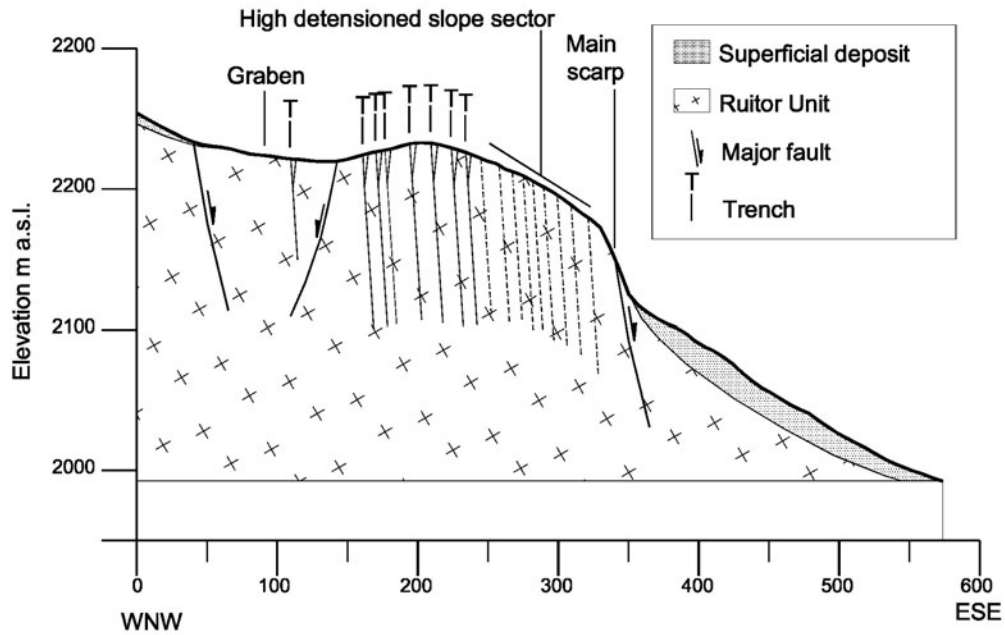


Figure 6.13: Geological section C-C' in the Arp Vieille sector.

Joint Set	Dip Direction	Range of variation	Dip	Range of variation
K1	110°	±20°	80°	±15°
K2	190°	±20°	90°	±10°
K3	000°	±15°	30°	±15°
K4	150°	±10°	85°	±15°
K5	55°	±10°	80°	±10°
K6*	55°	±5°	35°	±10°
Schistosity	235°	±5°	45°	±15°

* K6 joint set has a dip direction and dip angle very similar to those measured for the schistosity.

Table 6.3: Range of properties of joint sets on Arp Vieille area.

internal portion of the ridge, to the slope (N-W direction) in the more external sector. The instability at the toe of the scarp allows for the destressing upslope thus generating a system of deep and wide trenches along the sub-vertical discontinuity set. These structures are partially hidden by the presence of disoriented and disordered blocks toppled from the faces of the wider trenches.

6.6.4 Bochat section (D-D'). Geological setting

The geologic cross section D-D' (Figure 6.14) located on the southern portion of the DSGSD, in the Bochat area, is trending WNW-ESE and has a total length of about 1200 m from the reservoir (1700 m a.s.l.) to elevation 2100 m a.s.l.. The trend of the section is E37°S. The joint set data which characterise this portion of the landslide are shown in Table 6.4.

In the upper part, the section crosses a secondary ridge characterized by the presence of well developed trenches, depressions and back-facing scarps. These morphological structures are similar to those observed in other sectors of the Beauregard Landslide, for example along the Bochat Ridge. Some of them are morphological expressions of sub-vertical normal faults developed along K1 and K4 discontinuity sets. All the morphostructures described (faults, open cracks and trenches) widespread along the Bochat ridge are related to a brittle deformation pattern affecting the rock mass. This is characterized by crack initiation along the joints and the schistosity planes and a progressive propagation inside the rock mass due both to freeze-thaw cycles and to the pressure exerted by the material upslope. It is important to highlight that such sub-vertical normal faults do not lead to flexural toppling or block toppling mechanisms as for the Bochat Ridge and Arp Vieille area. Only rock fall instabilities are recognized along the steeper cliffs.

The Bochat area was investigated by seismic refraction surveys and borehole drilling. The S2/04 borehole was drilled on the road along the lake in Menthieu area (Figure 6.14). The subsurface data obtained identify a well developed shear zone (up to 12 m thick), at 150 m depth, characterized by the presence of a highly fractured rock (Figure 6.15). According to the seismic results, the cataclastic level has been interpreted as the prosecution towards the southern DSGSD portion of the shear zone recognized at depth in the S1/04 and S1-2/03 boreholes. Following this interpretation the main instability mechanism is related to the mechanical characteristics of the fractured and cataclastic materials which constitute the shear zone. Hence, in such a sector of the DSGSD, the shear zone can be interpreted as a compound surface along which the slope is mobilized. The faults developed along the main discontinuities can probably be connected to the basal shear zone assuming a listric geometry.

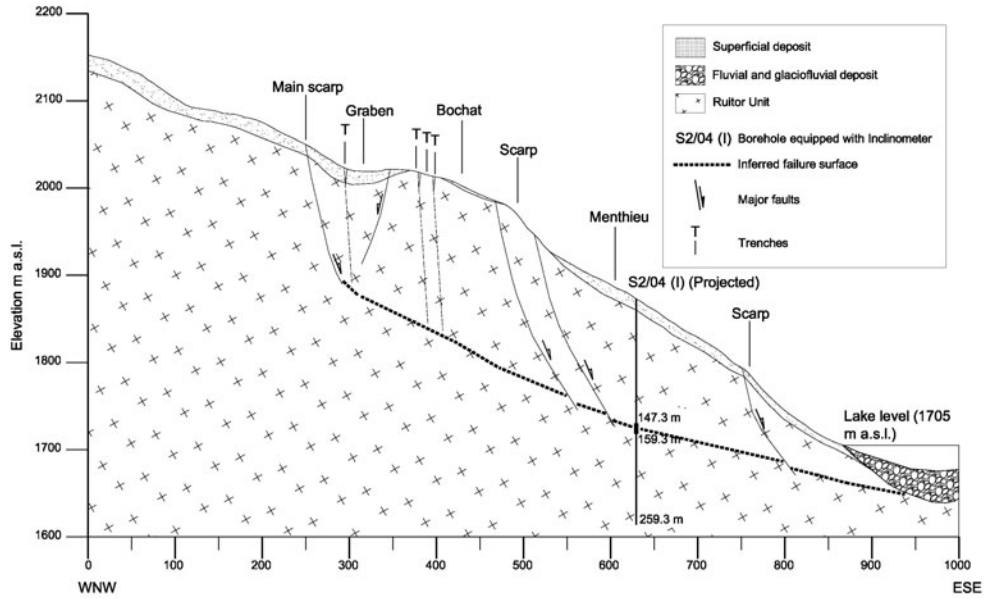


Figure 6.14: Geological section D-D' in the Bochat area.

Joint Set	Dip Direction	Range of variation	Dip	Range of variation
K1	110°	±20°	80°	±15°
K2	190°	±20°	90°	±10°
K3	000°	±15°	30°	±15°
K4	150°	±10°	85°	±15°
K5	55°	±10°	80°	±10°
K6*	55°	±5°	35°	±10°
Schistosity	200°	±30°	30°	±15°

* K6 joint set has a dip direction and dip angle very similar to those measured for the schistosity.

Table 6.4: Range of properties of joint sets on Bochat area.

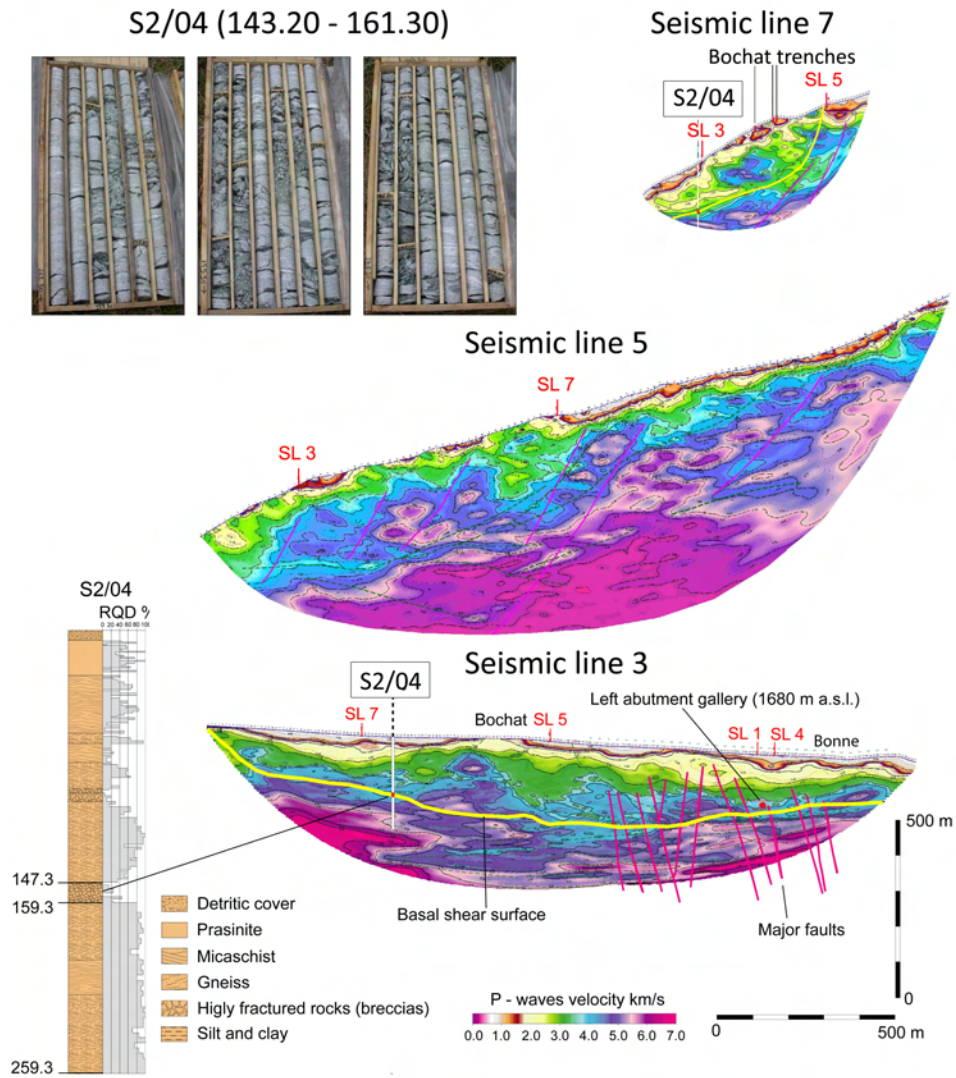


Figure 6.15: Site investigations results with indication of the main shear zone across borehole S2/04 (Bochat area) and interpretation of seismic refraction tomographic lines 3, 5 and 7 (Barla et al. 2010aa, modified).

6.6.5 Bonne-Alpettaz-Scavarda section (E-E'). Geological settings

The landslide sector which impinges on the arch dam has been extensively studied in the last few years. Recent advances in the monitoring work performed comprise the use of the ground based interferometric synthetic aperture radar (GBInSAR) system to investigate the upper portion (Alpettaz-Scavarda) of the slope.

Based on the displacement field obtained with the GBInSAR monitoring, a novel interpretation of the movements taking place in the three slope sectors (upper, central and lower one, Figure 6.3) was given (Barla et al., 2010a). The occurrence of a non-homogeneous deformation pattern characterized by higher displacement rates in the upper slope (Scavarda ridge) and slow and steady deformations along the basal portion of the landslide, suggests two different trends of behaviour for the two sectors.

The displacement pattern developing in the upper portion of the slope (Scavarda Ridge), which is related to the opening of tension cracks and slope bulging is evidence of a progressive translational movement along an incipient basal rupture surface. Beneath the Scavarda ridge, between 2300 and 2500 m a.s.l. elevation, the total displacements are in the range of 45 mm over 4 months. As shown in Figure 6.16, a stepped geometry of the rupture surface may be controlled by the sub-vertical faults and by schistosity planes dipping towards E-SE.

The behaviour of the slope at the toe, which impinges directly on the dam, is instead related to the geotechnical characteristics of the cataclastic rock forming the basal shear zone of the landslide, at 250m depth (see Figure 6.16), which is known to exhibit a time dependent behaviour. The movement patterns of this sector of the DSGSD show a small displacement rate of 4–6 mm/year, i.e. creep movements which are likely to be related to the seasonal fluctuations of the water table in the slope, resulting in changes of the effective stresses along the basal shear zone.

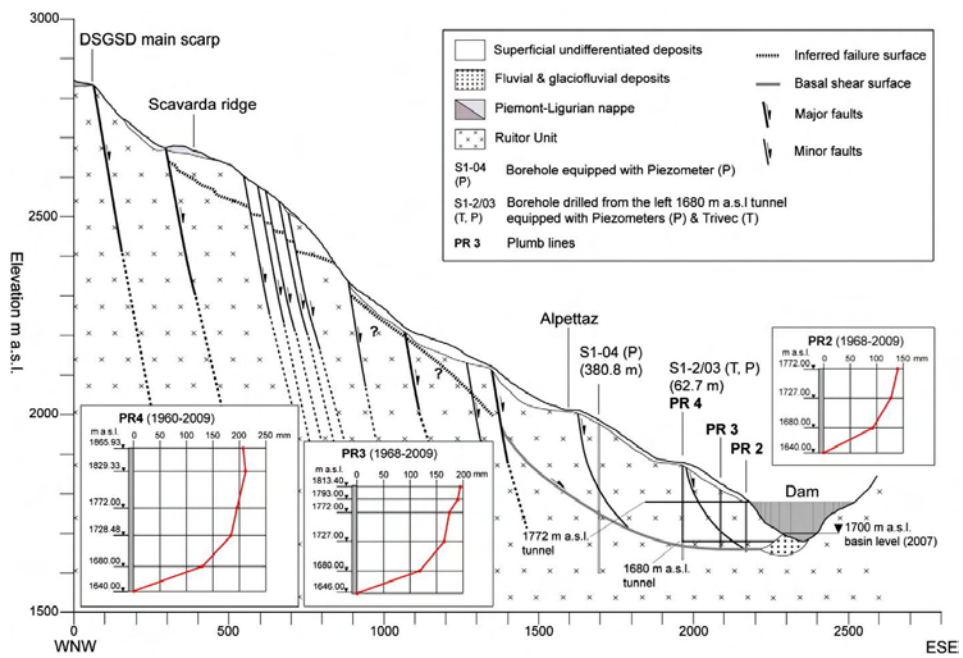


Figure 6.16: Geological section E-E' with indication of the cumulated displacement measured along the plumb lines installed on the slope (Barla et al., 2010a).

6.7 Summary

The Beauregard Landslide has relevant implications from the civil protection points of view. The landslide has been long studied because of its interaction with an arch gravity dam. Moreover, the continuous monitoring of the slope over a time span of more than 50 years has allowed to gain insights into the understanding of the behaviour not only of the basal portion of the slope, interacting with the dam, but also of the other sectors of the slope.

In this work the attention is posed on the S-W portion of the DSGSD where some key modes of instability have been identified. In the Bochat area, the opening of tension cracks and trenches is evidence of a progressive translational movement along an incipient basal surface, in the upper portion, whereas in the lower portion, a shear zone has already developed. This shear zone can be considered as the continuation of the shear zone observed in the Bonne sector of the DSGSD. The monitoring data indicate a rate of movement of 11-14 mm/year, whereas in the Bonne sector, the landslide shows slow movement (3-4 mm/year).

Flexural toppling and local block toppling are typical failure mechanisms observed in the middle portion of the landslide, for example in the Bochat Ridge and in the Arp Vieille area. These mechanisms are related to the two main discontinuity sets which characterise the landslide; the first one strikes parallel to the valley, the second one is perpendicular to it. These two discontinuity sets are widespread in the landslide and cause wide open trenches. Also the schistosity influences the potential development of instability. The rock mass is actually comprised of micashists and gneiss, which are characterised by marked strength anisotropy. In the Bochat Ridge, block toppling failure develops along the schistosity planes. Flexural and block toppling is mainly forced by the freeze-thaw cycles, whereas the movements in the Bochat area are related to seasonal fluctuations of the piezometric level in the slope.

References

- Barla, G. (2009).** “Long-term behaviour of the Beaugard dam (Italy) and its interaction with a deep seated gravitational slope deformation. Invited Keynote Lecture.” In “5th Colloquium, Rock Mechanics - Theory and Practice,” Vienna University of Technology.
- Barla, G. (2010).** “Progress in the understanding of deep-seated landslides from massive rock slope failure.” In “ISRM International Symposium and 6th Asian Rock Mechanics Symposium New Delhi, India,” .
- Barla, G., Antolini, F., Barla, M., Martinotti, M., Mensi, E., and Piovano, G. (2009a).** “Progetto MONIMOD. Relazione sul secondo anno di attività.” Technical report, Dipartimento di Ingegneria Strutturale e Geotecnica del Politecnico di Torino.
- Barla, G., Antolini, F., Barla, M., Martinotti, M., Mensi, E., and Piovano, G. (2009b).** “Progetto MONIMOD. Relazione sul terzo anno di attività.” Technical report, Dipartimento di Ingegneria Strutturale e Geotecnica del Politecnico di Torino.
- Barla, G., Antolini, F., Barla, M., Mensi, E., and Piovano, G. (2010a).** “Monitoring of the Beaugard landslide (Aosta Valley, Italy) using advanced and conventional techniques.” *Engineering Geology*, 116: 218–235.
- Barla, G., Antolini, F., Barla, M., Mensi, E., and Piovano, G. (2011).** “Integration of Ground-Based Radar interferometry and conventional techniques for monitoring the Beaugard deep-seated landslide.” In “8th International Symposium on Field Measurements in GeoMechanics. Berlino, 12-16 Settembre 2011,” .
- Barla, G., Ballatore, S., Canella, G., Amici, R., and Chiappone, A. (2005).** “La deformazione gravitativa di Beaugard e la sua interazione con una grande diga ad arco gravità.” In “Questioni di Ingegneria Geotecnica. Scritti in onore di Arturo Pellegrino. A Cura di G. Urciuoli.”, Hevelius Edizioni srl, Benevento.

- Barla, G., Ballatore, S., Chiappone, A., Frigerio, A., and Mazzà, G. (2006).** "The Beauregard Dam (Italy) and the deep seated gravitational deformation on the left slope." In "Hydropower 2006 - International Conference," pages 99–112. Kunming, China.
- Barla, G., Barla, M., and Martinotti, M. (2010b).** "Development of a new direct shear testing apparatus." *Rock Mechanics and Rock Engineering*, 43: 117–122.
- Barla, G. and Chiappone, A. (2006).** "Interazione tra deformazioni gravitative profonde di versante e impianti idroelettrici in ambiente alpino. Le dighe di Beauregard e Pian Palu." In "MIR Ciclo di Conferenze di Meccanica e Ingegneria delle Rocce, Politecnico di Torino," .
- Barla, G., Piovano, G., and Barla, M. (2008a).** "Progetto MONIMOD. Relazione di aggiornamento delle misure riguardanti la DGPV di Beauregard e la sua interazione con la diga." Technical report, Dipartimento di Ingegneria Strutturale e Geotecnica del Politecnico di Torino.
- Barla, G., Piovano, G., and Barla, M. (2008b).** "Progetto MONIMOD. Relazione di aggiornamento delle misure riguardanti la DGPV di Beauregard e la sua interazione con la diga." Technical report, Dipartimento di Ingegneria Strutturale e Geotecnica del Politecnico di Torino.
- Barla, G., Piovano, G., Barla, M., and Martinotti, M. (2007).** "Progetto MONIMOD. Relazione sul primo anno di attività." Technical report, Dipartimento di Ingegneria Strutturale e Geotecnica del Politecnico di Torino.
- Desio, A. (1973).** *Geologia applicata all'ingegneria. 3a Edizione.* Hoepli, Milano.
- Kalenchuk, K., Hutchinson, D., Diederichs, M., Barla, G., Barla, M., and Piovano, G. (2010).** "Three-dimensional mixed continuum-discontinuum numerical simulation of the Beauregard Landslide." In "European Rock Mechanics Symposium, Lausanne, Switzerland," pages 639–642.
- Martinotti, M. (2010).** *Creep behaviour of cataclastic rock in massive rock slopes.* Ph.D. thesis, Politecnico di Torino, Dottorato di Ricerca in Ingegneria per la Gestione delle Acque e del Territorio.
- Miller, S., Barla, G., Piovano, G., and Barla, M. (2008).** "Geotechnical and temporal risk assessment of a large slope deformation." In "42nd US Rock Mechanics Symposium and 2nd U.S.-Canada Rock Mechanics Symposium, San Francisco (USA)," .

Chapter 7

Realistic simulation of key instabilities of the Beauregard massive landslide

7.1 Introduction

Numerical modelling of the instability modes which characterise the Beauregard Landslide will be discussed in the following. The four FDEM models presented are based on the geological models described in the previous chapter. The aim of the analyses is to apply the “total slope failure” approach to the recognised failure mechanisms which characterize the S-W portion of the landslide on the upstream side far from the dam body and to highlight the possible development features.

7.2 Geotechnical parameters of rock mass and discontinuity sets

Based on field investigations, laboratory tests and the geological model described in the previous chapter, the geotechnical model of the left slope along the Bonne-Alpettaz-Scavarda section has been set up by Barla et al. (2006). This model considers (Figure 7.1):

- the rock mass which comprises intact rock (schists and micaschists) and joints;

- the faults and cataclastic zones;
- the shear zone (soil like material with silt and clay).

The geotechnical parameters of the different geological features included have been derived from the results of the laboratory tests performed (intact rock, natural and artificial joints, soil-like material from the main shear zone) and the application of the Geological Strength Index (GSI) to the various rock mass conditions (I: good quality rock mass, undisturbed and blocky; II, III: poor quality rock mass, weak and disturbed landslide body containing crushed rock and soil like material). The constitutive laws used in the numerical analysis are also indicated.

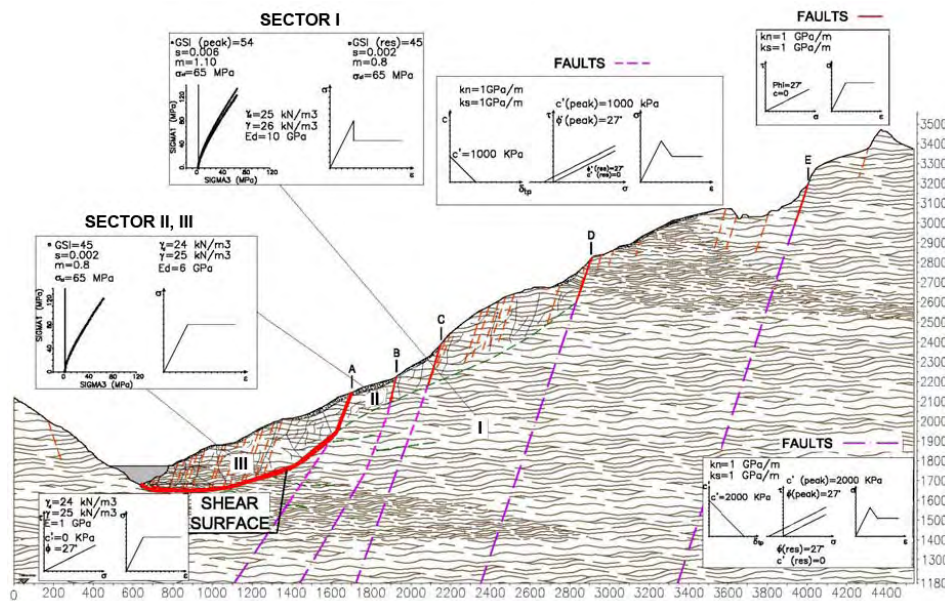


Figure 7.1: Cross section of the slope near to the dam with indication of the main geological features, the constitutive laws, and the corresponding geotechnical parameters adopted in the numerical modelling (GSI=Geological Strength Index; σ_{ci} =intact rock uniaxial compressive strength; m, s =Hoek-Brown rock mass parameters; E_d =rock mass deformation modulus; c', ϕ' =rock mass/joint cohesion and friction angle; k_n, k_s =normal and tangential joint stiffness; γ_d, γ_s =dry, saturated rock mass unit weight) (from Barla et al. (2006)).

7.3 Bochat ridge section (A-A')

Numerical modelling studies of the Bochat ridge section (A-A') have been carried out using the two dimensional FEM code Phase² v.7 and the FDEM code Y2D, based on the geological model described in Chapter 6. The aim of the analyses was to evaluate the potential mechanisms driving to instability. Generally, it has been observed that the stability is affected by the trenches (K1, K2 or K4 joint sets), the sub-horizontal joint set K3 and the schistosity. The range of dip and dip direction for these joint sets is shown in Table 7.1. A joint network was generated using a feature introduced in the Phase² code, which allows one to reproduce two dimensional networks of joints and to simulate patterns of natural jointing in rock masses. Joint networks can be generated according to a statistical model with user-defined statistical distributions for the joint spacing, length and persistence.

Joint Set	Dip Direction	Range of variation	Dip	range of variation
K1	100°	±20°	80°	±15°
K2	185°	±20°	90°	±10°
K3	000°	±15°	30°	±15°
K4	140°	±10°	80°	±15°
K5*	55°	±10°	80°	±10°
K6	55°	±5°	35°	±10°
Schistosity	195°	±30°	30°	±15°

* K5 joint set has a pluridecametric spacing.

Table 7.1: Range of dip and dip direction of main joint sets which characterise the Bochat Ridge.

7.3.1 FEM model setup and modelling results

Two models of the Bochat ridge section (A-A') were set up:

1. the *K4-schistosity* model, which comprises the K4 joint set, representing the trenches, and the schistosity;
2. the *K2-K3* model, with the K2 and K3 joint sets, where K2 is a secondary subvertical joint set, orthogonal to the valley axis, and K3 represents the cross-joints dipping into the slope.

***K4-schistosity* model**

The geometry and mesh of the *K4-schistosity* model are shown in Figure 7.2. The size of the model is 525 m wide and 222 m high. The mesh adopted consisted of 47954 elements and 29742 nodes with a nominal element size of the finite element mesh of 2 m. Plane-strain conditions were assumed, whereas the boundary conditions were: zero x-displacement on the sides and zero x and y-displacement at the bottom. Initial in situ stress conditions were based on a horizontal to vertical stress ratio (k) of 0.43.

The parameters of interest for the FEM model are: rock mass deformability and strength; discontinuity orientation, spacing and persistence. The rock type in the zone of interest is gneiss and micaschist. The rock mass strength of the blocks is based on the geologic strength index GSI=54 which characterises the rock mass belonging to Sector I (see Figure 7.1). The rock mass behaves according to the Hoek-Brown constitutive model with parameters listed in Table 7.2.

The joint network was generated using the “randomize” tool, in order to generate a parallel statistical joint network using a different sampling of the random variables (i.e. spacing, length, and persistence) as already mentioned above. The orientations of joint sets introduced in the FEM model are listed in Table 7.4 together with the trend plane of the cross section.

The mechanical parameters (friction angle, dilation angle, cohesion, and tensile strength) of joint sets and schistosity were chosen according to the available geotechnical model and given in Table 7.3. Joint normal stiffness and joint shear stiffness were varied in proportion to the elastic modulus of the rock mass.

Figure 7.3 shows the FEM results of simulation for the *K4-schistosity* model, in terms of total displacements and yielded elements. Also the deformed mesh is illustrated; it is noted that the displacements involve all the slope and the overall stability is affected due to unfavourable orientation of discontinuities.

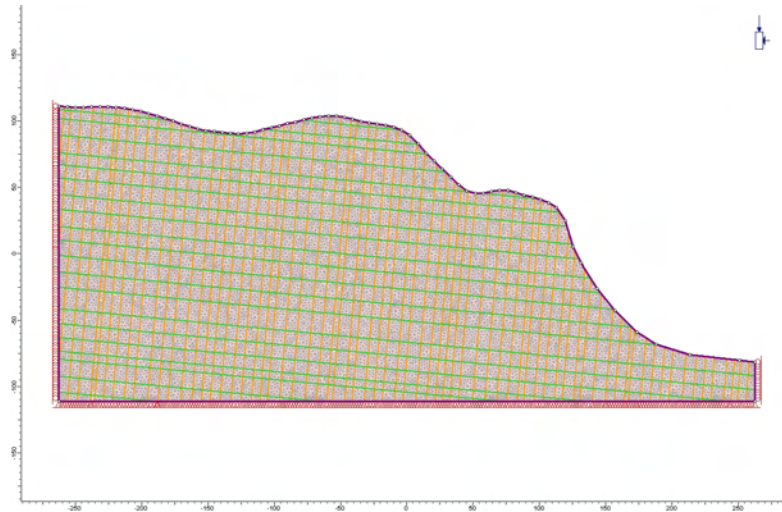


Figure 7.2: Basic slope geometry and mesh used in the FEM analyses. *K4-schistosity* model.

<i>Rock mass (gneiss - micaschist)</i>	
UCS, Uniaxial Compressive Strength (MPa)	65
GSI, Geologic Strength Index	54
Density (kg/m ³)	2500
Young's modulus (MPa)	10000
Poisson's ratio (-)	0.3
Failure criterion	Hoek-Brown
m_b parameter	1.1
s parameter	0.006
Residual m_b parameter	0.8
Residual s parameter	0.002

Table 7.2: Rock mass deformability and strength properties.

<i>Joint set 1 (K2-K4)</i>		<i>Joint set 2 (schistosity and K3)</i>	
Tensile strength σ_t (MPa)	0	Tensile strength σ_t (MPa)	0
Cohesion c (MPa)	0.04	Cohesion c (MPa)	0.03
Friction angle φ ($^\circ$)	27	Friction angle φ ($^\circ$)	22

Table 7.3: Main joint sets and schistosity strength properties for FEM models.

	<i>Joint set 1 (vertical joint K1)</i>	<i>Joint set 1 (vertical joint K4)</i>	<i>Joint set 2 (schistosity)</i>
<i>Joint model</i>	Parallel statistical	Parallel statistical	Parallel statistical
<i>Orientation</i>			
Trace plane dip direction ($^\circ$)	36	36	36
Dip ($^\circ$)	85	85	15
Dip Direction ($^\circ$)	260	310	195
<i>Spacing</i>			
Mean (m)	7	7	10
Distribution	Normal	Normal	Normal
St. Dev. (m)	2	2	2
Rel. Min. (m)	5	5	6
Rel. Max. (m)	8	8	12
<i>Length</i>	Infinite	Infinite	Infinite
<i>Joint End Condition</i>	All Closed	All Closed	All Closed

Table 7.4: Joint network setting for the *K4-schistosity* model.

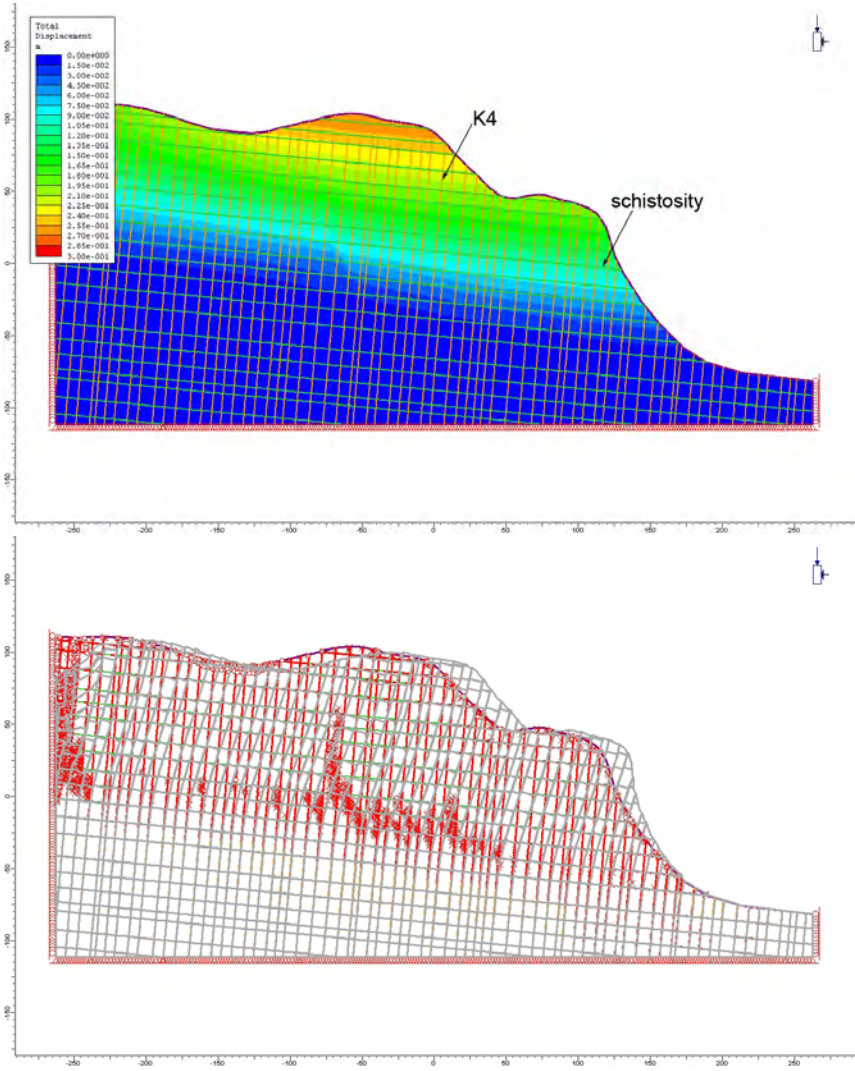


Figure 7.3: Total displacements and yielded elements at the end of the FEM analysis (*K4-schistosity* model). Deformed mesh is also shown. The *K4* and the schistosity orientation is unfavourable to stability.

K2-K3 model

The K2-K3 model was discretised as shown in Figure 7.4: the mesh consisted of 47748 elements and 28861 nodes, with a nominal element size of 2 m. The boundary conditions adopted are vertical displacements fixed at the bottom while horizontal displacements are restrained along the vertical boundaries. The mechanical properties assigned to the rock mass and joints are given in Table 7.2 and 7.3, respectively.

The joint network parameters are shown in Table 7.5. The overall stability of the slope is influenced by the unfavourable orientation of K2 (dip dir 5°/dip 80°) and K3 (dip dir 15°/dip 15°) joint sets. Actually, the FEM analyses did not provide a solution when those joint sets were considered. Yielded elements are located on the main slope scarps as illustrated in Figure 7.5. The deformation contour of the slope is also indicated.

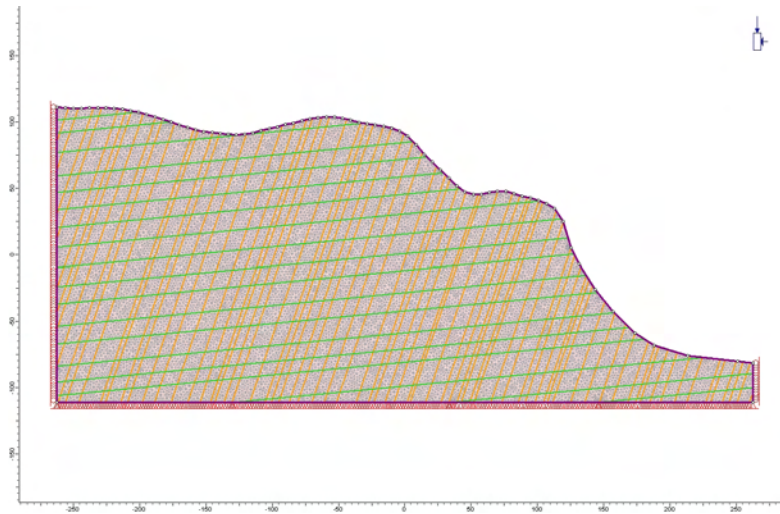


Figure 7.4: K2-K3 model: geometry and mesh adopted in the FEM analysis.

Based on FEM computation, the joints affecting the rock slope stability are the schistosity when dipping out of the slope, and the trenches represented by the sub-vertical sets K1 and K4, when dipping into the slope. Actually, in such cases, the FEM analyses did not converge within the total number of iterations assigned. The FEM analyses also show that instability develops when two secondary joint sets (K2 and K3) are considered.

Basically, the FEM analyses indicate that the order of magnitude of the total displacements is equal to 10^{-1} m. A tensile zone is also observed in the upper region of the

	<i>Joint set 1 (vertical joint K2)</i>	<i>Joint set 1 (vertical joint K3)</i>
<i>Joint model</i>	Parallel statistical	Parallel statistical
<i>Orientation</i>		
Trace plane dip direction (°)	36	36
Dip (°)	80	15
Dip Direction (°)	5	15
<i>Spacing</i>		
Mean (m)	7	12
Distribution	Normal	Normal
St. Dev. (m)	3	3
Rel. Min. (m)	5	10
Rel. Max. (m)	15	20
<i>Length</i>	Infinite	Infinite
<i>Joint End Condition</i>	All Closed	All Closed

Table 7.5: Joint network setting for the K2-K3 model.

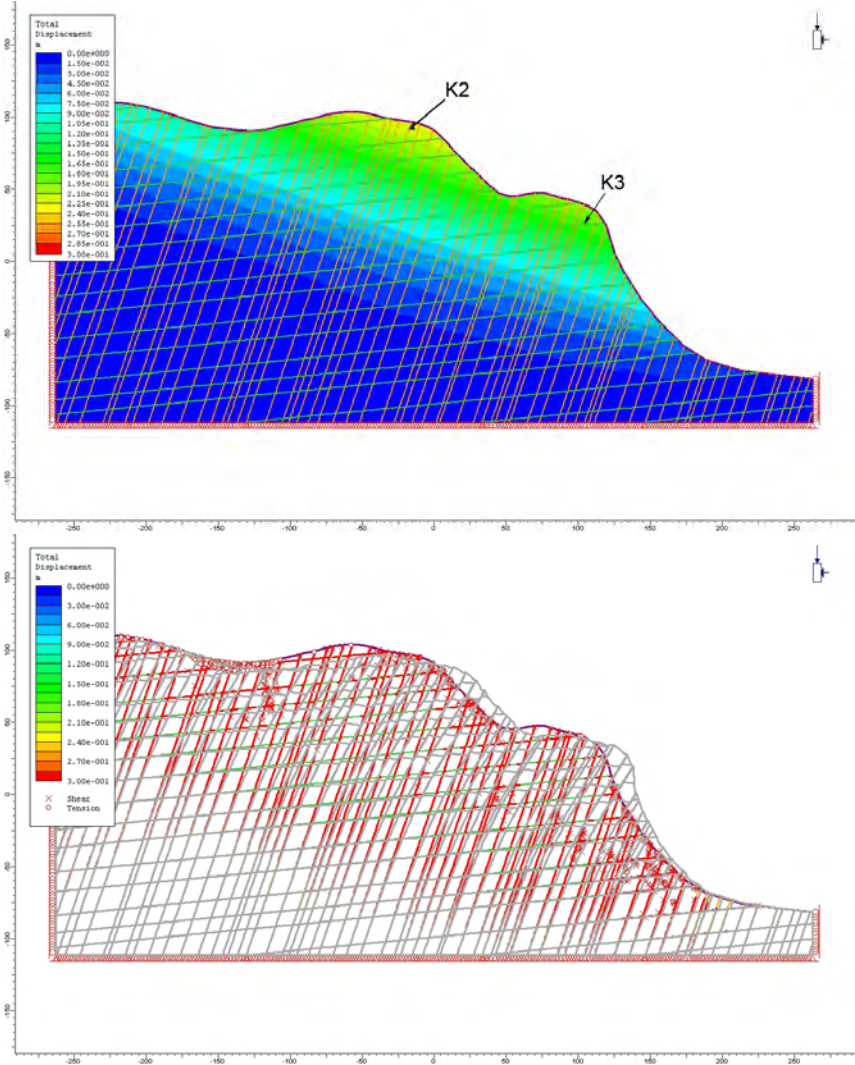


Figure 7.5: Total displacements and yielded elements at the end of the FEM analysis (K2-K3 model). Deformed mesh is also shown. The K2 and K3 orientation is unfavourable to stability.

slope (graben) and many yielded sub-vertical joints and yielded sub-horizontal joints are shown at the base of the slope. Some yielded elements are also shown inside the slope.

7.3.2 FDEM model setup and modelling results

The FDEM model of Section A-A' was set up according to the FEM model just illustrated. The mesh and boundary conditions are consistent with those adopted with FEM, except for some adjustment of the joint network in the lower portion of the slope to avoid thin triangular elements which may lead to numerical instability during fracture simulation.

The Mohr-Coulomb criterion, which controls the behaviour of the rock mass, requires the following parameters: elastic modulus, Poisson's ratio, internal friction angle, dilation angle, internal cohesion, and tensile strength (Table 7.6). The joint contact of pre-existing discontinuities is also represented by the Mohr Coulomb constitutive model. This requires the following input parameters: friction angle, cohesive strength, and tensile strength (Table 7.7).

<i>Intact material properties</i>	
Elastic modulus, E (GPa)	10
Poisson's Ratio, ν	0.3
Density, ρ (kg/m ³)	2500
Internal cohesion, c_i (MPa)	2.75
Internal friction angle, φ_i (°)	27
Dilation angle, ψ (°)	0
Tensile strength, σ_t (MPa)	3 ÷ 7
Fracture energy release rate, G_f (J/m ²)	150
<i>Numerical parameters</i>	
Viscous damping (kg/ms)	2.00E+07
Normal contact penalty (GPa)	10
Tangential contact penalty (GPa)	1
Fracture penalty (GPa)	10

Table 7.6: Rock mass properties and numerical parameters used in the FDEM study.

The numerical simulations were performed in two stages: 1) set the initial stress conditions, 2) simulate the instability of the slope. The first stage was run with the intent to reproduce the initial state of stress within the slope with no fracturing being allowed

between the finite elements. The fracture process was activated during the second stage with the intent to simulate the slope instability. During both stages computation was led to equilibrium. Figure 7.6 shows the decrease of the total kinetic energy during Stage 1 for the *K4-schistosity* model; complete equilibrium is reached, with the number of cycles equal to $20 \cdot 10^6$ with a time step size of $1 \cdot 10^{-6}$. Considering that the Y2D code is computer demanding, the elastic analysis required a significant computation time (12 days) on a 2.33 GHz, 8 GB RAM pc. On the same computer, the Stage 2 required 8 days of computation.

<i>Joint set 1 (K1-K2-K4)</i>		<i>Joint set 2 (schistosity and K3)</i>	
Tensile strength σ_t (MPa)	0	Tensile strength σ_t (MPa)	0
Cohesion c (MPa)	0.04	Cohesion c (MPa)	0.03
Friction angle φ ($^\circ$)	27	Friction angle φ ($^\circ$)	22

Table 7.7: Main joint sets and schistosity strength properties for FDEM models.

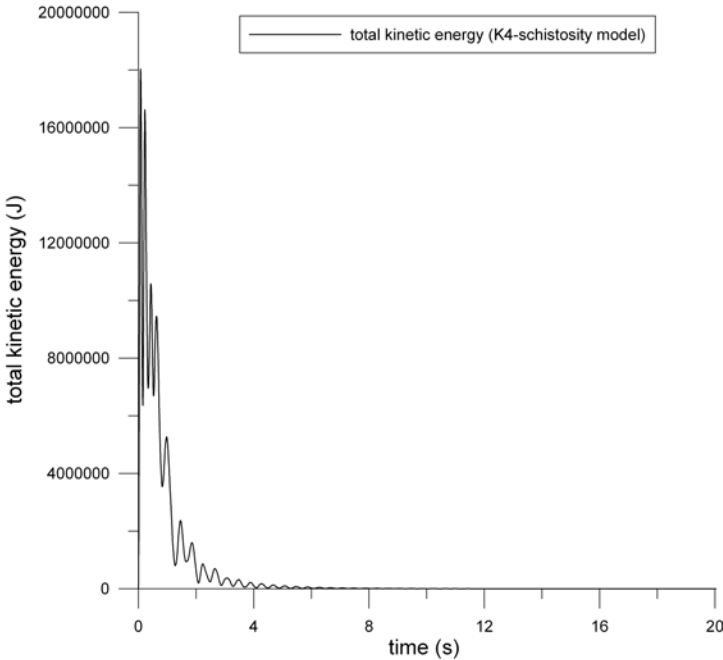


Figure 7.6: Total kinetic energy during Stage 1 of the FDEM simulation (*K4-schistosity* model).

K4-schistosity model

Figure 7.7 and 7.8 illustrate the FDEM simulation of instability. The two models are different in terms of the rock mass tensile strength, which was assumed equal to 7 MPa and 3 MPa, respectively. The analyses have highlighted that as the rock mass strength increases, the flexural toppling failure involves higher columns. This is illustrated in Figure 7.7 which shows the development of a hinge zone at a depth of 80-100 m. Shorter columns at the base of the slope bend slightly and slide along the schistosity plane, allowing the movement of the upslope longer columns. The schistosity plane does not influence the motion of the upslope columns as new fractures develop due to the columns which bend out of the slope. This type of failure can be recognised as flexural toppling. Slopes undergoing flexural toppling often self-stabilize once the discontinuities rotate to a sufficiently shallow dip angle. In this model the area of movement is concentrated near the lower main scarp and decreases significantly upslope. On the contrary, when the rock mass strength is low, the amount of movement increases. As illustrated in Figure 7.8 a deep highly fractured zone develops, allowing failure of a massive portion of the slope.

K2-K3 model

The FDEM analyses were also carried out introducing the K2 and K3 joint sets and the results are shown in Figure 7.9. Fracturing develops from the base of the slope to the upper scarp; however, only the frontal portion of the main scarp is characterized by a major destressing of the rock mass which leads to local instability. The K2 and K3 joint sets will be favourable to block toppling observed in the frontal portion of the Bochat Ridge. The FDEM results were obtained after a first elastic stage which required 15 days of computation time on a 2.33 GHz, 8 GB RAM pc. On the same computer, the second stage required 9 days of computation.

Figure 7.10 shows typical views of the Bochat Ridge from the right slope of the valley, the dam site and the N-W portion of the left slope at 2500 m a.s.l. elevation. The general view highlights an extensive area covered by a thick talus which results from an old rock avalanche; the talus is partly forested in the N-E portion (Figure 7.11), at the toe of the main scarp, whereas in the S-W portion it is less vegetated. The Bochat Ridge is characterised by morpho-structural features typical of a deep-seated landslide, such as a bulging toe and a ridge top spreading (Figure 7.10). In the upper part of the ridge a series of wide trenches belonging to the K1 and K4 joint sets are observed. Figure 7.12 shows these linear and deeply cuts, expression of extensional opening of a vertical or downward dipping surface. Evidences of a progressive movement towards the lake have been highlighted from the monitoring system: the GPS targets (GPS4-GPS6-GPS7)

located above the Bochat Ridge show movements toward S-E; the total station targets which monitor the displacements of the base of the main scarp and the bulging toe near the lake, record a progressive movement of the slope toward the lake. The horizontal displacements are observed to be 5 times the vertical displacement.

The numerical results obtained highlight that stability is mainly influenced by the trenches (K1-K4 joint system). FDEM modellings observation and monitoring results show that this portion of the landslide is characterised by flexural toppling leading to the formation of large-scale slope deformations. This is well demonstrated by the screenshots in Figure 7.8. If a weaker rock mass is considered, first a thick zone of fractures develops inside the slope, at a depth of about 80-100 m; then, as progressively block toppling develops on the main scarp, flexural toppling occurs and develops along a wide portion of the slope. Antislope scarps develop and gaps open between the columns. The instability results in sliding along a shallow surface (Figure 7.8).

The rock mass structure is seen to be also dominated by discontinuities (K3) parallel with the schistosity, dipping to N-E. According to the FDEM results (Figure 7.9), a local instability develops on the main scarp of section A-A' with a thick talus at the toe of the cliff as observed in situ and now covered with trees.

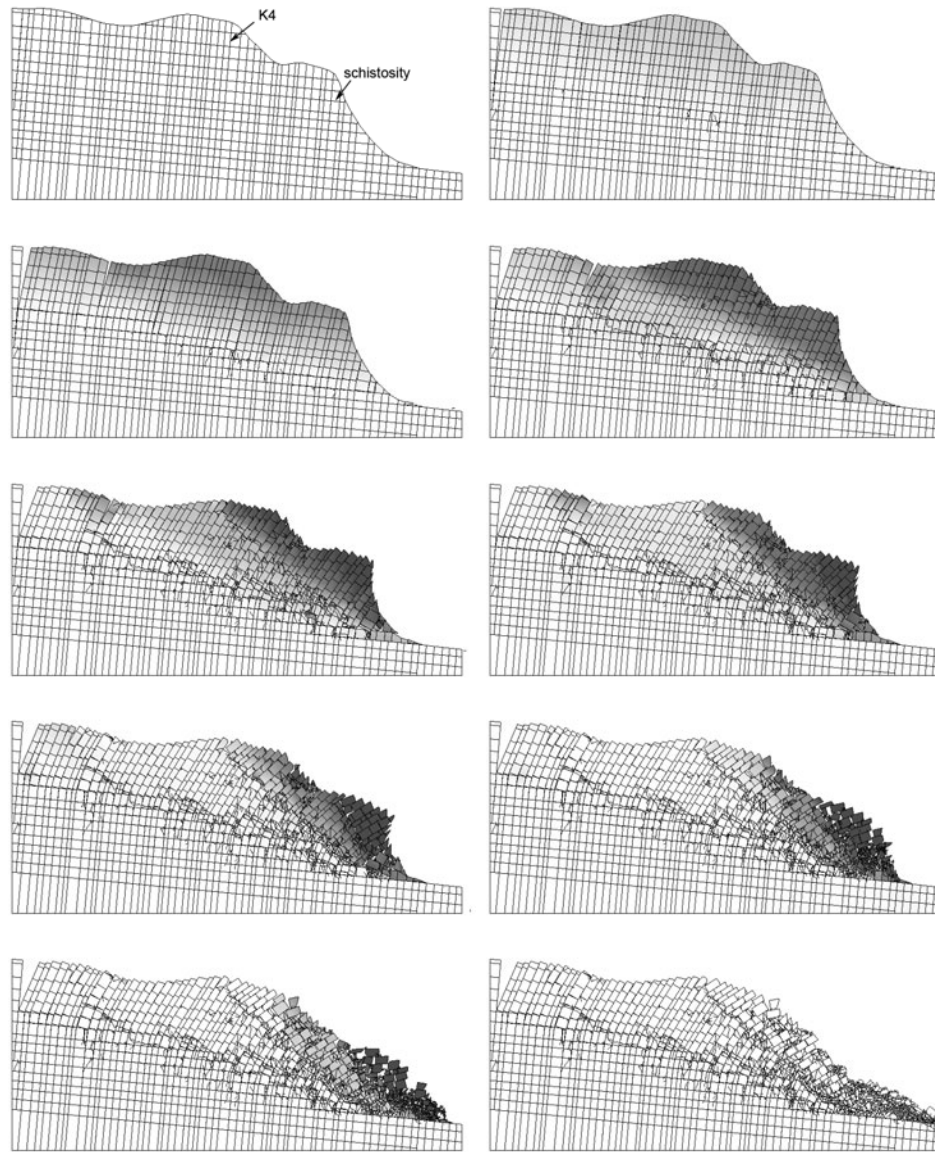


Figure 7.7: Subsequent screenshots of the instability simulated with Y2D code (K4-schistosity model) for $\sigma_{t,rock\ mass}=7$ MPa.

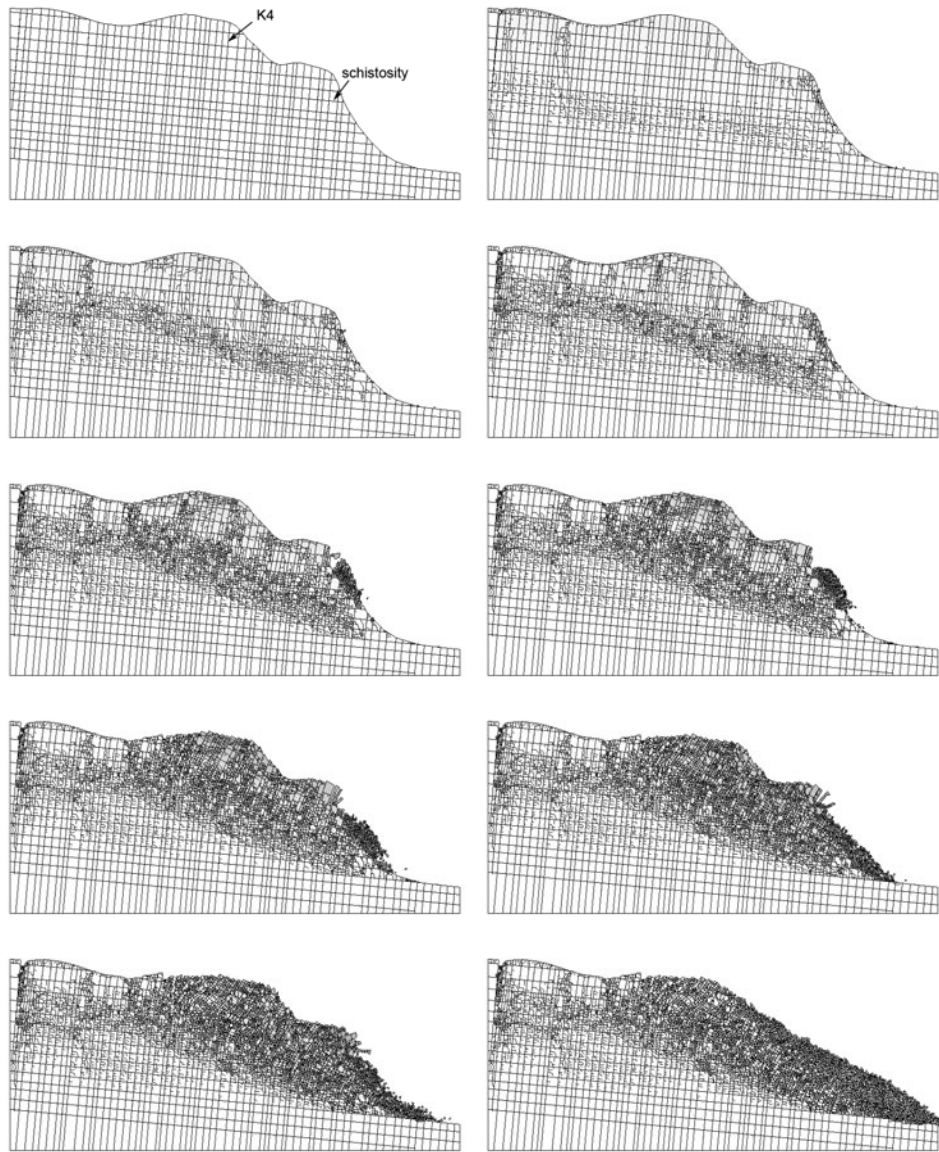


Figure 7.8: Subsequent screenshots of the instability simulated with Y2D code (K4-schistosity model) for $\sigma_{t,rock\ mass}=3$ MPa.

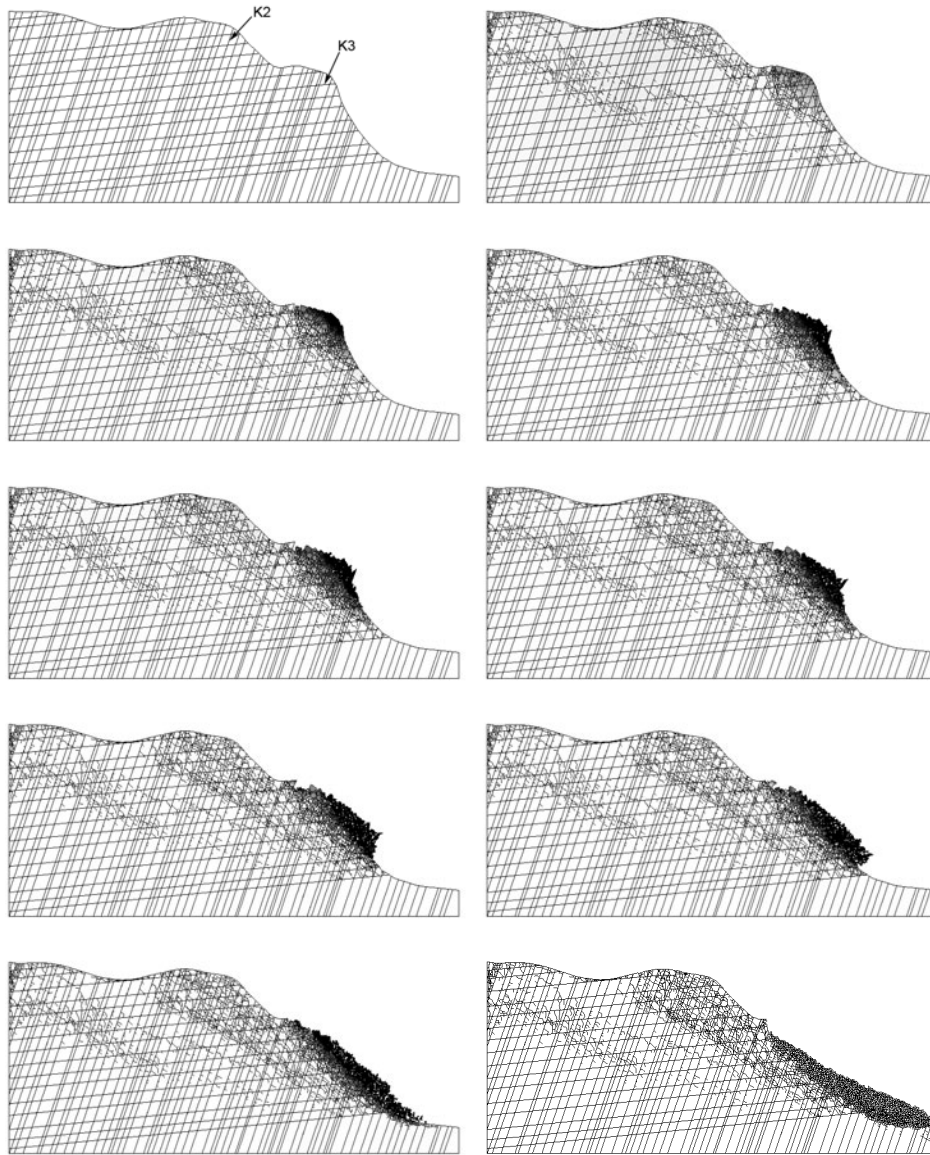


Figure 7.9: Subsequent screenshots of the instability simulated with Y2D code (K2-K3 model) for $\sigma_{t,rock\ mass}=3$ MPa. K2 and K3 orientation is unfavourable to local stability of the main scarp.

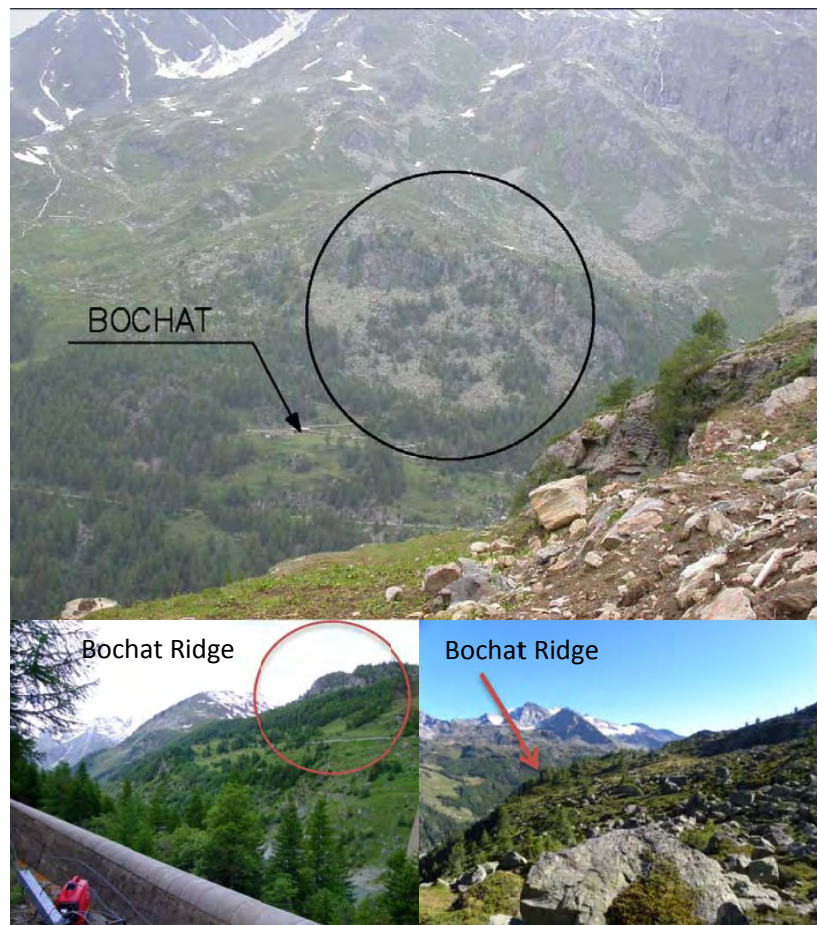


Figure 7.10: View of the Bochat Ridge from the opposite side of the Valgrisenche Valley and the rock blocks at the toe of the main scarp (black circle). View of the Bochat Ridge from the dam site (lower left photo) and from N-W (lower right photo).



Figure 7.11: Photos of the thick talus located at the toe of the Bochat Ridge.



Figure 7.12: Trenches in the upper part of the Bochat Ridge represented by the K1-K4 joint sets.

7.4 Bochat ridge section (B-B')

The B-B' cross section has been built to reproduce the block toppling instability clearly observed on the Bochat Ridge. The frontal portion of the main scarp is indeed characterised by block toppling failures. According to the geological model, blocks partially slide along the schistosity planes dipping S-W (inclination 35-40°) and partially break in tension along the K3 planes dipping N-E (inclination 25-30°). The K4 joint set together with K2 has an important role in the development of this type of failure, as they are vertical joints which generate the blocks (Figure 7.13).

The main joint sets present in the Bochat Ridge area and their orientation are listed in Table 7.1. The rock outcrop of Figure 7.14 shows the main discontinuity sets. The block toppling model comprises a good rock mass quality and includes cross-joints (schistosity). It is to be noted that no toppling would occur in this model without the cross-joints, because of the high rock strength that inhibits the bending of columns.



Figure 7.13: Particular of the photo of the Bochat Ridge taken from the S-W margin of the talus. The rock joints are representative of the main discontinuity sets at the site.



Figure 7.14: The main discontinuity sets at the Bochat Ridge.

According to the geological interpretation and observation of block toppling, two main joint sets have been chosen: the vertical joint set dipping 80° into the slope (trenches orthogonal to the valley axis), with joints spaced 1 m apart, and the schistosity plane dipping 30° out of the slope. Although a pervasive schistosity is present, a mean spacing of 4 m is considered (K3, which also influences stability, has spacing ranging between 2 and 5 m), in order to simulate the blocky structure of the rock mass. To set the spacing, the kinematic test of toppling instability has been also carried out.

If a block on an inclined rock surface is considered, the nature of the instability is dependent on the block geometry and the angle of friction between the block and the surface on which it is resting. Four options are shown in Figure 7.15, as the various regions in a graph of block aspect ratio versus friction angle. To establish the equilibrium due to toppling, consider the location of the line of action of the force due to gravity. This passes through the centre of gravity of the block and will coincide with the lower apex of the block if $b/h = \tan\psi$, which is the limiting equilibrium condition. Thus, toppling will not occur if $b/h > \tan\psi$, and will occur if $b/h < \tan\psi$.

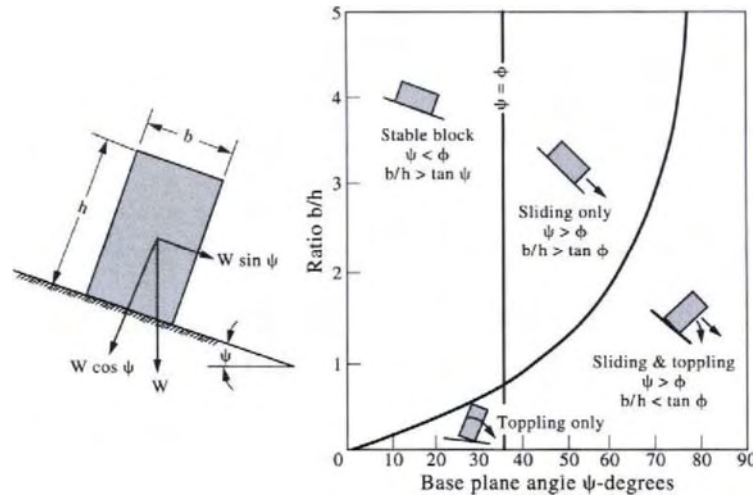


Figure 7.15: Sliding and toppling instability of a block on an inclined plane (from Hudson and Harrison, 1997).

7.4.1 FEM model setup and modelling results

The geometry of the slope was imported in Phase² and meshed with a nominal element size of 0.5 m. The size of the model is 70 m wide and 60 m high, and the mesh adopted consisted of 23047 elements and 14582 nodes (Figure 7.16). Initial in situ stress conditions were based on a horizontal to vertical stress ratio (k) of 0.43. Plane-strain conditions were assumed. The boundary conditions specified were: zero x-displacement at the sides and zero x and y-displacement at the base. The rock mass deformability and strength parameters are listed in Table 7.2.

The parallel statistical joint network inserted in the FEM model was generated using a different sampling of the random variables such as spacing, length, and persistence (Table 7.8). The trend plane of the cross section was also set (section B-B' has a trend plane N29°E). The friction angle, dilation angle, cohesion, and tensile strength of the main joint sets are summarised in Table 7.9. Joint normal stiffness and joint shear stiffness were varied in proportion to the deformability modulus of the rock mass.

The high persistence of cross-joints is shown to have a dramatic effect on the slope behaviour. The FEM analysis was unstable and the convergence was not established within the total number of iterations; a landslide from block toppling failure developed. Figure

7.17 shows the FEM results of numerical simulation in term of total displacements. Also the deformed mesh and the yielded joints are illustrated. The movement is concentrated in the upper section of the slope.

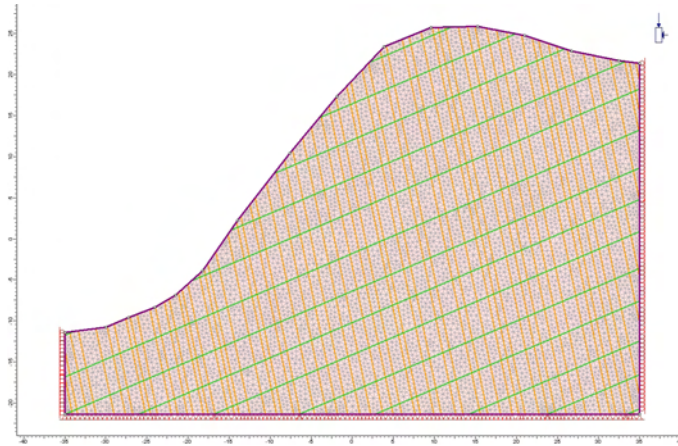


Figure 7.16: Basic slope geometry used in the FEM analysis (section B-B'). The main joint set dips at 80° ; the sub-vertical joint mean spacing is 1m; the schistosity joint set dips at 30° and its mean spacing is 4 m.

If a value of spacing equal to 1 m and 2 m is set for the vertical joint set and the schistosity, respectively, the instability mechanism observed in the FEM analysis is quite different. The instability mode is now sliding along the schistosity planes (Figure 7.18).

	<i>Joint set 1 (vertical joint K2)</i>	<i>Joint set 2 (schistosity)</i>
<i>Joint model</i>	Parallel statistical	Parallel statistical
<i>Orientation</i>		
Trace plane dip direction (°)	299	299
Dip (°)	80	30
Dip Direction (°)	25	195
<i>Spacing</i>		
Mean (<i>m</i>)	1	4
Distribution	Normal	Normal
St. Dev. (<i>m</i>)	0.5	0.5
Rel. Min. (<i>m</i>)	0.5	1.5
Rel. Max. (<i>m</i>)	1.5	5
<i>Length</i>	Infinite	Infinite
<i>Joint End Condition</i>	All Closed	All Closed

Table 7.8: Section B-B': joint network setting.

	<i>Joint set 1 (vertical joint K2)</i>	<i>Joint set 2 (schistosity)</i>
Normal stiffness k_n (MPa/m)	100000	100000
Shear stiffness k_s (MPa/m)	10000	10000
Slip Criterion	Mohr-Coulomb	Mohr-Coulomb
Tensile strength σ_t (MPa)	0 (tension positive)	0.01 (tension positive)
Cohesion c (MPa)	0.04	0.03
Friction angle φ (°)	27	22

Table 7.9: Natural joints and schistosity strength properties used in the FEM numerical analyses.

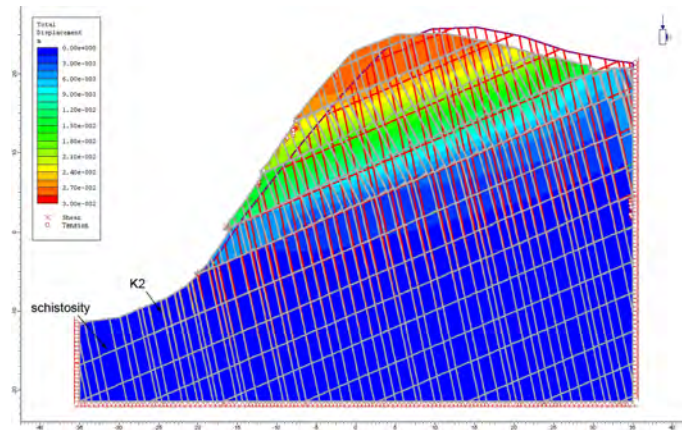


Figure 7.17: Total displacements, yielded elements and joints at the end of the FEM analysis (section B-B'); deformed model is also shown.

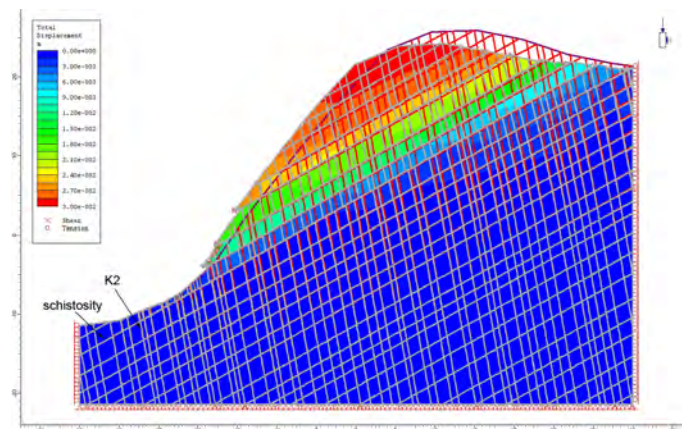


Figure 7.18: FEM model of section B-B' with a lower value of spacing for the schistosity. Total displacements, yielded elements and joints at the end of the simulation.

7.4.2 FDEM model setup and modelling results

The FDEM model of section B-B' was built according to the FEM model. The mesh and boundary conditions are consistent with those adopted with FEM (Figure 7.16), but the pre-existing joints are introduced only in the upper part of the model, that is the area subjected to maximum displacements in the FEM analysis.

The necessary condition to avoid numerical instability during fracturing simulation, lead to a manual correction of the mesh adopted in order to eliminate bad triangular geometry. Actually, the FDEM tool requires a regular mesh as much as possible. However, the elements size could be different, but thin triangular elements are not allowed.

The rock mass behaves according to the Mohr-Coulomb criterion which requires the following parameters: elastic modulus, Poisson's ratio, internal friction angle, dilation angle, internal cohesion, and tensile strength (Table 7.6). The Mohr-Coulomb model was also adopted for the pre-existing joints (Table 7.7).

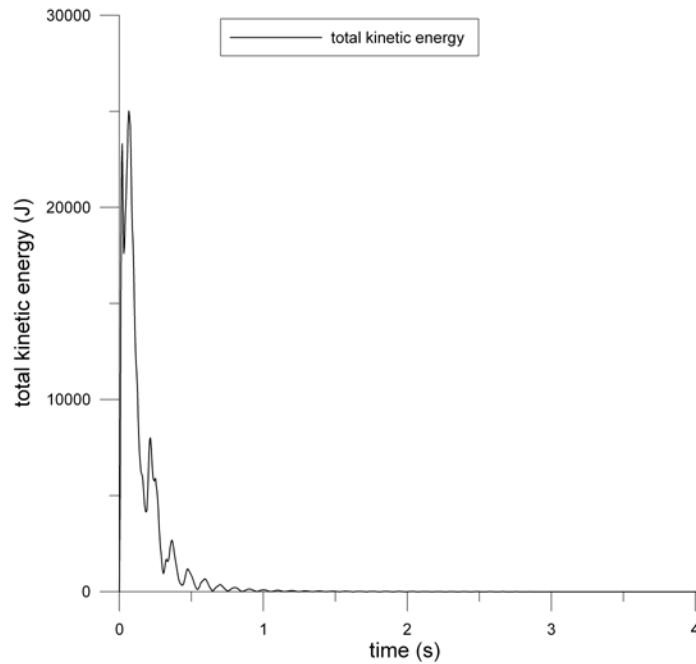


Figure 7.19: Total kinetic energy during Stage 1 in the FDEM simulation (section B-B').

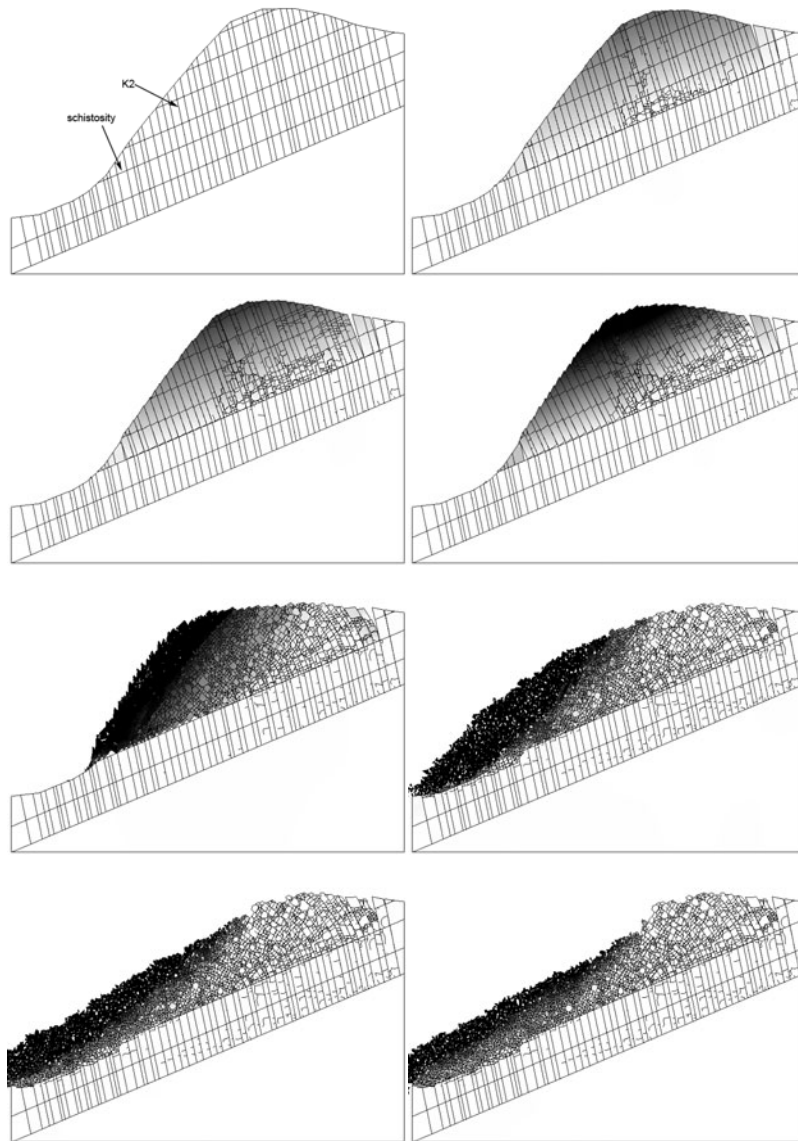


Figure 7.20: Block deformation plots for a slope with rock mass tensile strength of 3 MPa. FDEM simulation.

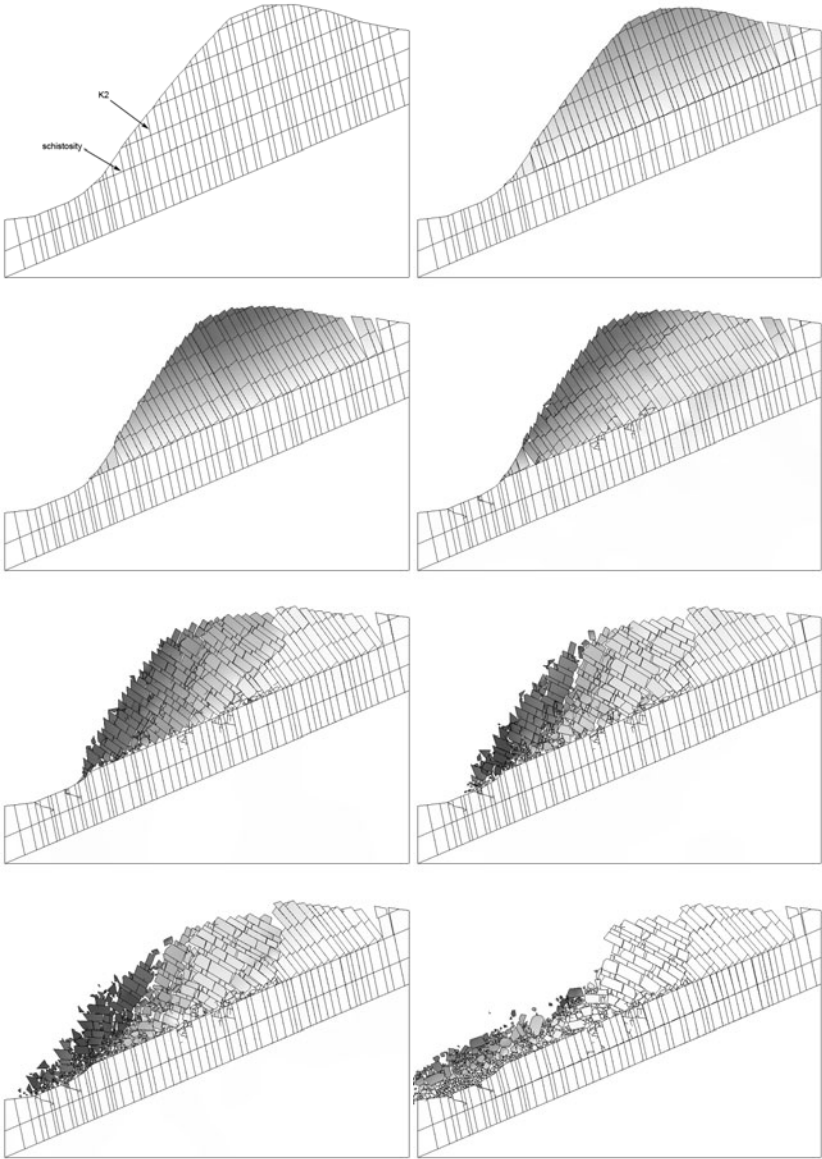


Figure 7.21: Block deformation plots for a slope with rock mass tensile strength of 7 MPa. FDEM simulation.

As usual, the numerical simulations were performed in two stages. The first stage was run with the intent to reproduce the initial state of stress within the slope with no fracturing being allowed between the finite elements. The fracture process was activated during the second stage to assess the slope stability. During both stages computation was led to equilibrium; Figure 7.19 shows the total kinetic energy versus the simulation time during the first stage. The total kinetic energy of the system has to be largely reduced in order to obtain the computed vertical stresses close to the expected theoretical values. Considering the limited size of the model, the first stage computation time was of 4 days; complete equilibrium was reached, with the number of cycles equal to $4 \cdot 10^6$ with a time step size of $1 \cdot 10^{-6}$. The second stage computation time was 5 days.

Two models were setup. They are different in the tensile strength assumed for the rock mass. The block toppling slope instability when the rock mass has a tensile strength of 3 MPa is shown in Figure 7.20, whereas the block deformation for a tensile strength of 7 MPa is illustrated in Figure 7.21.

The destressing of the slope is related to the foliation and schistosity which dip towards S-W; other joints occurring sub parallel to the slope surface (K3) are related to the destressing taking place in the slope. The occurrence of toppling movement is evidenced by the presence of a number of tension cracks (Figure 7.22) and assemblies of rotated blocks, roughly ordered according to the fabric of the toppled mass. They cover part of the wide trench perpendicular to the valley axis as shown in Figure 7.22.

In the FDEM numerical simulation, cross-joints (schistosity) were added with continuity equal to 100%; as shown by the numerical results, the deformation of the slope is controlled by the cross-joints; in the first case most of the movement takes place in the upper portion of the slope where rock columns undergo bending and overload the lower blocks. In the lower part of the slope, the columns are progressively sliding. Some fractures start inside the slope and as the columns rotate, the cross-joints no longer form continuous planes in the upper portion of the slope, so they are no more free to slide and the movement progressively is reduced. Due to the persistence of the cross-joints, the FDEM simulation shows a catastrophic block toppling taking place. Similar catastrophic failure mechanisms were observed in the second FDEM model including a fully persistent cross-joint set with an higher rock mass strength.



Figure 7.22: View of block toppling toward S-W from the top of the Bochhat Ridge. A wide trench perpendicular to the valley and belonging to K2 joint set is shown.

7.5 Arp Vieille section (C-C')

A numerical modelling study of section C-C' has been carried out following the procedure illustrated for section A-A'. The potential driving mechanism of the instability has been evaluated. Combinations of discontinuity orientation were examined to determine if specific failure modes are possible. The range of dip and dip direction for each joint set is shown in Table 7.10.

Generally, the stability is influenced by the trenches which belong to K1 or K4 joint system, the schistosity and the subhorizontal K3 joint set. The joints network was generated as illustrated in the previous analyses.

Joint Set	Dip Direction	Range of variation	Dip	Range of variation
K1	110°	±20°	80°	±15°
K2	190°	±20°	90°	±10°
K3	000°	±15°	30°	±15°
K4	150°	±10°	85°	±15°
K5	55°	±10°	80°	±10°
K6*	55°	±5°	35°	±10°
Schistosity	235°	±5°	45°	±15°

* K6 joint set has a dip direction and dip angle very similar to those measured for the schistosity.

Table 7.10: Range of dip and dip direction of main joint sets which characterise the Arp Vieille area.

7.5.1 FEM model setup and modelling results

The model set up for the Arp Vieille area comprises the K1 joint set and the schistosity. The geometry of the model with the mesh and the boundary conditions adopted, is illustrated in Figure 7.23. The nominal element size of the finite element mesh was 3 m and the mesh adopted consisted of 33161 elements and 22266 nodes. The boundary conditions specified were: zero x-displacement on the sides and zero x and y-displacement at the base. The size of the model is 573 m wide and 302 m high. Initial in situ stress conditions were set with a horizontal to vertical stress ratio (k) of 0.43. Plane-strain conditions were assumed.

Rock mass strength and mechanical parameters of joint sets were chosen according to the geotechnical model (refer to Table 7.2 and 7.3).

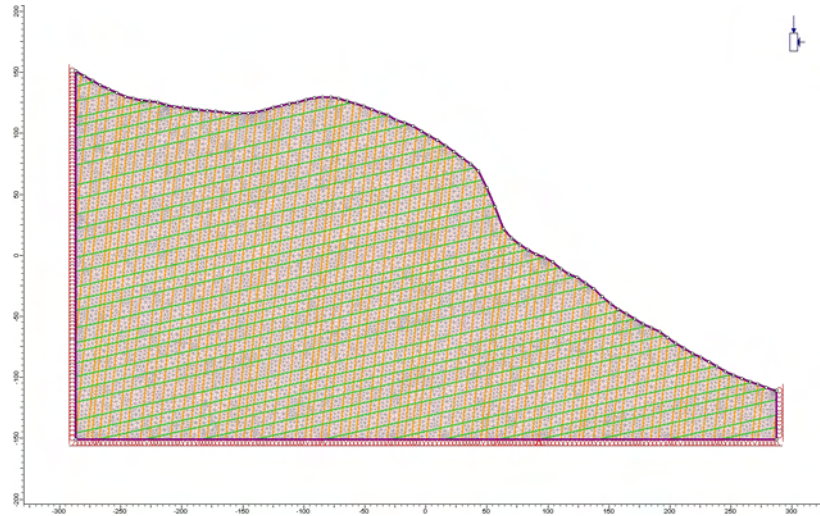


Figure 7.23: Basic slope geometry and mesh used in the FEM analyses (*K1-schistosity* model).

Based on FEM computation, the joints affecting the rock slope stability are mainly the trenches, i.e. the sub-vertical sets K1 and K4, when dipping into the slope; the schistosity and the K3 sub-horizontal planes do not influence stability, as generally they are dipping into the slope. For the mean planes of joints, FEM analysis were stable. However, with K1 and K4 having the orientation indicated in Table 7.11, the FEM analyses were unstable with no convergence being reached within the total number of iterations. It has been chosen to illustrate the numerical results obtained by introducing K1 and schistosity joint sets.

Figure 7.24 shows the FEM results when the rock mass is subdivided by the K1 and schistosity joint sets. The analysis were unstable. The results are shown in terms of total displacements and yielded elements. Also the deformed mesh is illustrated; displacements involve the entire slope so that stability is compromised. Yielded elements concentrate on the main scarp and inside the slope where a potential shear surface could form.

	<i>Joint set 1 (vertical joint K1)</i>	<i>Joint set 1 (vertical joint K4)</i>	<i>Joint set 2 (schistosity)</i>
<i>Joint model</i>	Parallel statistical	Parallel statistical	Parallel statistical
<i>Orientation</i>			
Trace plane dip direction (°)	42	42	42
Dip (°)	85	80	45
Dip Direction (°)	290	330	235
<i>Spacing</i>			
Mean (<i>m</i>)	7	7	10
Distribution	Normal	Normal	Normal
St. Dev. (<i>m</i>)	2	2	2
Rel. Min. (<i>m</i>)	5	5	6
Rel. Max. (<i>m</i>)	8	8	12
<i>Length</i>	Infinite	Infinite	Infinite
<i>Joint End Condition</i>	All Closed	All Closed	All Closed

Table 7.11: Joint network setting for section C-C'.

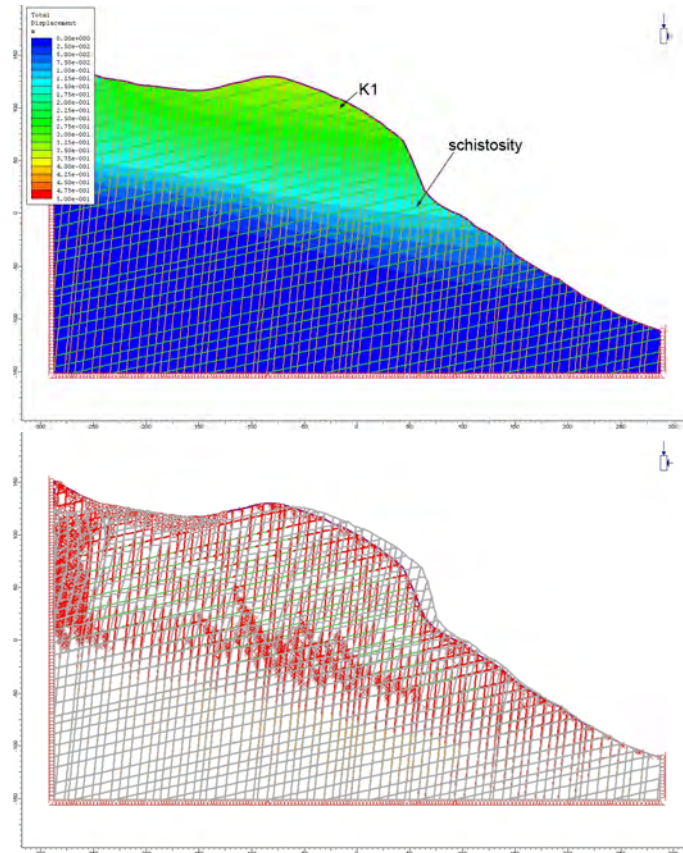


Figure 7.24: Total displacements and yielded elements at the end of the FEM analysis (*K1-schistosity* model). Deformed mesh is also shown. *K1* orientation is unfavourable to stability.

7.5.2 FDEM model setup and modelling results

The FDEM model of Section C-C' was built according to the FEM model. The mesh and boundary conditions were consistent with those adopted with FEM, except for some adjustment of the joint network to avoid numerical instability. The mechanical properties listed in Table 7.6 are given to the rock mass. Table 7.7 shows the mechanical properties of the cross-joints and trenches.

As usual, two stages of computation were performed, the first one to set the initial stress conditions, and the second to simulate the instability of the slope. The fracture process was allowed only in the second stage with the intent to assess the slope instability. As shown in Figure 7.25 where the total kinetic energy versus computation time is plotted, in the first stage the complete equilibrium is reached in $20 \cdot 10^6$ steps with a time step size of $1 \cdot 10^{-6}$. Considering that the Y2D code is computer demanding the elastic analysis required a significant computation time in terms of 20 days on a 2.33 GHz, 8 GB RAM pc. The Stage 2 required 11 days of computation.

FDEM simulation results are shown in Figure 7.26 and 7.27 for different values of the rock mass tensile strength. With a tensile strength of 7 MPa, the failure mechanism is a flexural toppling. First some new fracture develops inside the slope, then allowing the model to run, the columns undergo bending, much more upslope than at the base of the scarp. The deformation of the slope is mainly controlled by the sub-vertical joints (trenches). At the end of computation, a potential failure surface develops 120 m deep.

This portion of the Bochat Ridge shows a similar morphology with the N-E portion, due to the presence of the same trenches NE-SW trending. The main scarp is mainly vertical and in the outcrop in the forefront it is possible to recognise the main discontinuity sets and the apparent orientation of the foliation. A detail of the main vertical cliff and the vegetated talus is shown in Figure 7.28; evidence of rockfalls activity have been found limited to blocks which are falling freely from the cliff face. In the upper part of the slope, ridge-top trenches occur (Figure 7.29) belonging to K1 and K4 joint sets. In such an area, the rock mass weakened by flexural toppling could lead to a large-scale landslide as indicated by the numerical results shown in Figure 7.27.

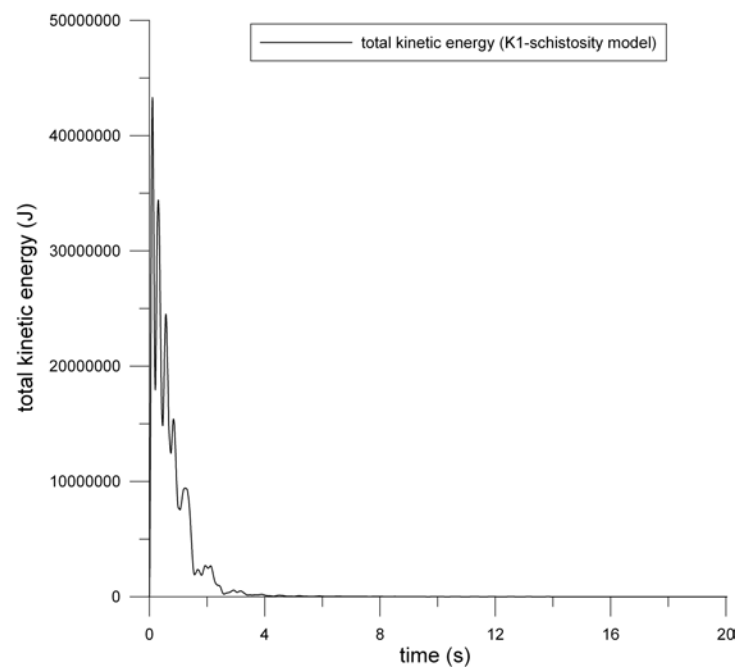


Figure 7.25: Total kinetic energy during Stage 1 in the FDEM simulation (*K1-schistosity* model)

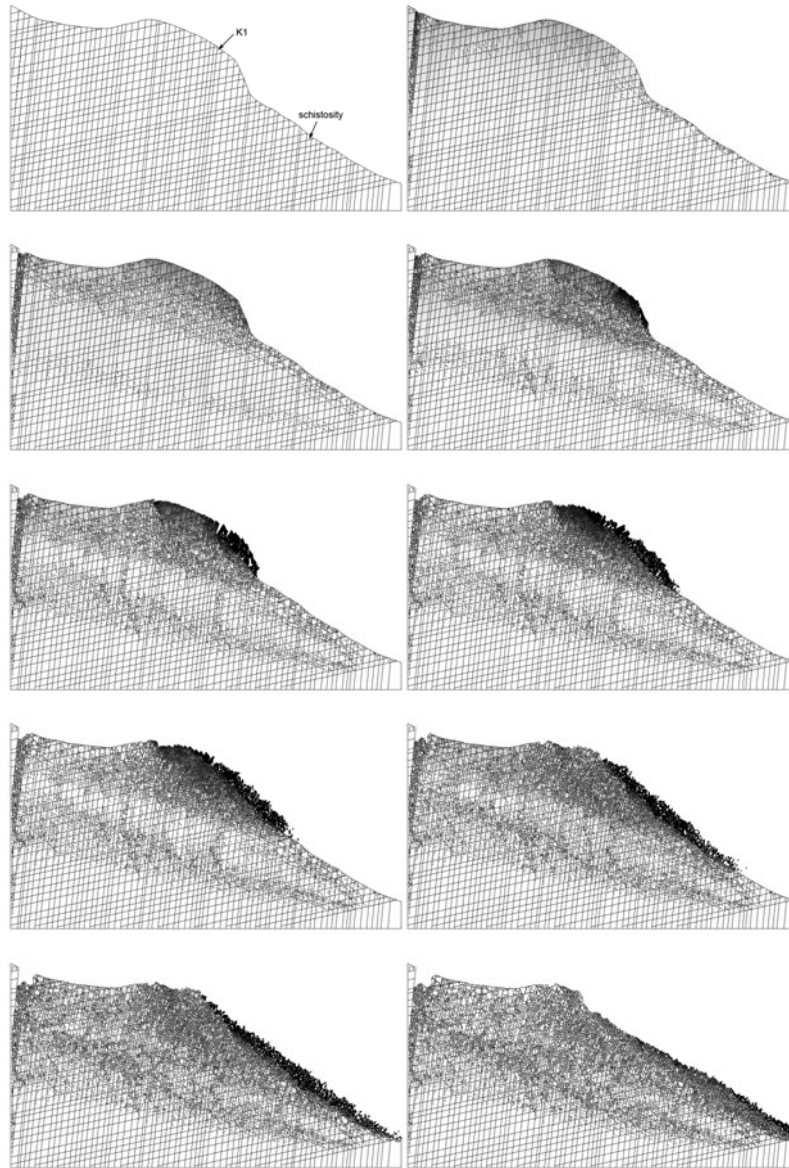


Figure 7.26: Subsequent screenshots of the instability simulated with Y2D code (K1-schistosity model) for $\sigma_{t,rock\ mass}=3$ MPa.

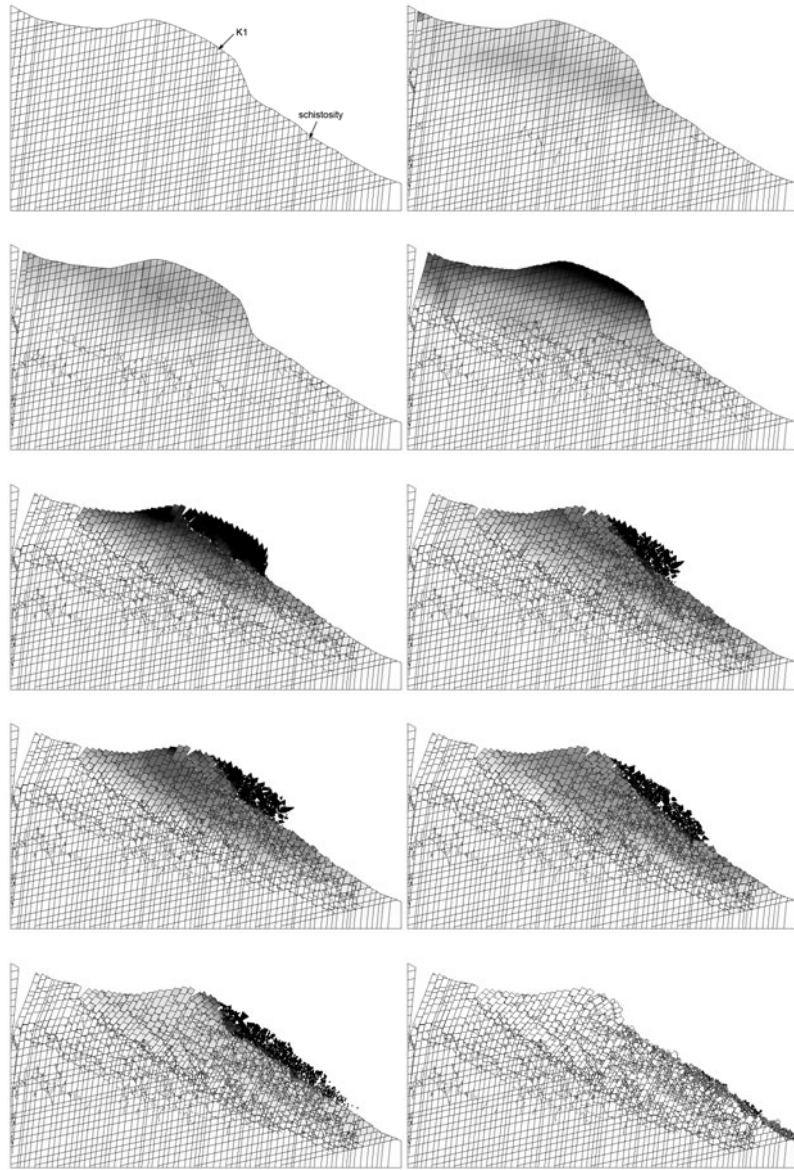


Figure 7.27: Subsequent screenshots of the instability simulated with Y2D code (K1-schistosity model) for $\sigma_{t,rock\ mass}=7$ MPa.



Figure 7.28: Details of the main scarp: vertical cliff where blocks are defined by the main joint sets.



Figure 7.29: View of the wide trenches (K1 and K4 joint sets) located above the crest.

7.6 Bochat section (D-D')

Numerical modelling studies of the Bochat section (D-D') have been carried out with the two dimensional FEM code Phase² v.7 and the FDEM code Y2D. As discussed in the previous chapter, a good level of understanding of the geological and geotechnical factors which influence the stability of the Bochat area has been available.

The aim of the numerical analyses was to evaluate the potential driving mechanism of instability and simulate the interaction between the upper and lower portion of the slope. The present study was conducted taking into consideration the previous modelling studies of section (E-E') which represent the landslide sector which impinges on the arch dam. Actually, the observed failure mechanism for the Bonne are and Bochat areas is similar, because in both sectors sliding occurs along a basal shear zone comprising cataclastic rock.

7.6.1 FEM model setup and modelling results

The geometry of the FEM model was based on the Bochat geological section illustrated in the previous chapter. The model included the rock mass in accordance with its quality condition, the sub-vertical trenches and the shear zone forming the basal failure surface. The geotechnical parameters of the different features included in the model are shown in Figure 7.1. The rock type in the zone of interest is gneiss and micaschist.

The rock mass belonging to Sector I (see Figure 7.1) is a good quality rock mass, undisturbed and blocky, and was introduced in the model to represent the deep rock mass. The moving mass was represented by rock belonging to Sector III, that is a poor quality rock mass, weak and crushed reduced to soil like material. The rock mass behaves according to the Hoek-Brown constitutive model with parameters listed in Table 7.12.

The shear zone was introduced in the model as a 12 m thick layer of material as shown in borehole S2/04 drilled in the Menthiu area. Such level of material was characterised by using Mohr-Coulomb failure criterion. The mechanical properties of the trenches and faults were similar to those of the shear zone. A Mohr-Coulomb failure criterion was used, with friction and cohesion values corresponding to the lower values obtained in the interpretation of laboratory tests (triaxial tests and direct shear tests) on the soil like material (cataclastic and shear zone material).

Two types of models were set up which are different in the geometry of the shear zone:

1. the *rigid-block* model is characterised by a rigid block failure mechanism;
2. the *circular surface* model is characterised by a sliding on a circular surface.

<i>Rock mass (gneiss - micaschist)</i>	<i>Sector I</i>	<i>Sector III</i>
UCS, Uniaxial Compressive Strength (MPa)	65	65
GSI, Geologic Strength Index	54	45
Density (kg/m ³)	2500	2400
Young's modulus (MPa)	10000	6000
Poisson's ratio (-)	0.3	0.3
Failure criterion	Hoek-Brown	Hoek-Brown
m_b parameter	1.1	0.8
s parameter	0.006	0.002
Residual m_b parameter	0.8	0.8
Residual s parameter	0.002	0.002
<i>Mohr Coulomb parameters</i>		
Friction angle φ (°)	27	25
Dilation angle ψ (°)	0	0
Cohesion c (MPa)	2.75	2.21

Table 7.12: Rock mass deformability and strength properties.

Initial in situ stress conditions were based on a horizontal to vertical stress ratio (k) of 0.43. Plane-strain conditions were assumed, whereas the boundary conditions were: zero x-displacement at the sides and zero y-displacement at the bottom. The size of the model is 995 m wide and 710 m high.

The geometry and mesh of the two models are shown in Figure 7.30. In the *rigid-block model* model, the mesh adopted consisted of 32814 finite elements and 16987 nodes with a nominal element size of the finite element mesh of 4 m. The overall mesh of the *circular surface model* model consisted of 32915 finite elements and 17020 nodes with an average size of elements equal to 5 m.

A number of parametric FEM analyses has been carried out in order to calibrate the numerical model and assess the stability condition. The Strength Reduction Factor was calculated for different values of the friction angle of the shear zone. The results for both the models are shown in Table 7.13. The values of friction angle adopted for the shear zone are based on the characterisation of shear material and previous numerical studies of the Beauregard landslide in the area close to the dam. At this point, it is worth to point out those studies (Barla et al. (2006), Barla (2009, 2010), Kalenchuk et al. (2010), Martinotti (2010) and Miller et al. (2008)).

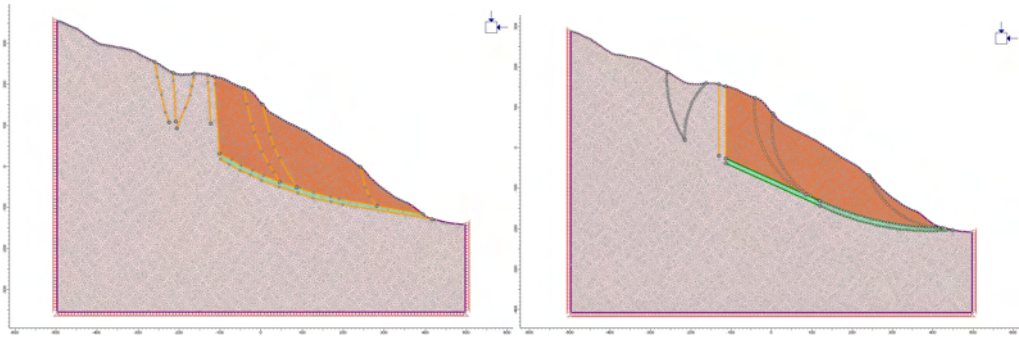


Figure 7.30: Basic slope geometry and mesh used in the FEM analyses of Bochat section (D-D'). On the left the *rigid-block model* model is shown, whereas, on the right the *circular surface model* is illustrated.

<i>Shear zone strength parameters</i>		<i>Rigid-block model</i>	<i>Circular surface model</i>
Friction angle φ (°)	Cohesion c (MPa)	SRF	SRF
27	0	1.3	1.19
23	0	1.1	1.01
22	0	1.06	0.97
21	0	1.01	-
19	0	0.91	-

Table 7.13: Computed Strength Reduction Factor in the FEM analyses.

Two dimensional modelling with Flac (FDM) and Phase² (FEM) codes was carried out to evaluate the stability of the slope. In the FDM and FEM modelling studies, with the basal sliding zone represented with parameters shown in Figure 7.1, the computations performed would lead to a safety factor ranging between 1.16 and 1.18. With a friction angle of 22° assumed for the sliding zone, the limit equilibrium condition would be reached with a computed safety factor equal to 1.07 (Barla, 2010). All these studies were performed by introducing the ground water table as monitored in the summer months (May/June to September/October).

Limit equilibrium stability analyses have also been performed with the method of slices and a stochastic approach (Miller et al., 2008). Results of slope stability analysis assuming a residual non linear shear-strength envelope and summer ground-water level, would lead to a factor of safety of 0.997. The residual shear-strength envelopes have friction angles of about 20° to 22°.

The FEM computations of the Bochat area basically validate the above results. It is worth mentioning that such analyses have been carried out under drained conditions. In the *rigid-block* model, the limit equilibrium condition was reached when the shear zone has a friction angle equal to 21° (Figure 7.31). A similar value of friction angle ($\varphi=23^\circ$) determined the limit equilibrium condition in the *circular surface* model. As shown in Figure 7.31, one cannot see any difference in the type of failure between the two FEM models.

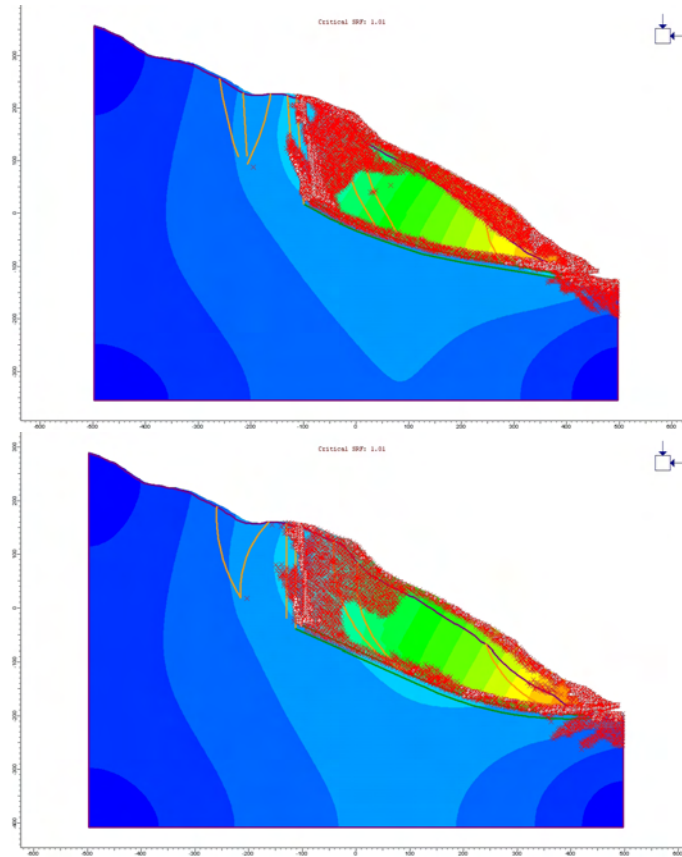


Figure 7.31: Phase² model (FEM) with near limit equilibrium parameters along the basal shear zone for *rigid-block* model (left) and *circular surface* model (right).

7.6.2 FDEM model setup and modelling results

Two dimensional modelling was also carried out with FDEM to study the evolution of the instability and the interaction between the moving mass forming the lower portion of the slope and its upper portion. The models were set up with the same geometry, mesh and boundary conditions as the FEM ones. The mechanical properties of the rock mass, shear zone and trenches were not varied respect to the FEM model. Such properties are shown in Table 7.14 and Table 7.15 together with the numerical parameters introduced in the FDEM modelling.

<i>Intact material properties</i>	<i>Sector I</i>	<i>Sector II</i>	<i>Shear zone</i>
Elastic modulus, E (GPa)	10	6	6
Poisson's Ratio, ν	0.3	0.3	0.3
Density, ρ (kg/m ³)	2500	2400	2400
Internal cohesion, c_i (MPa)	2.75	2.21	0
Internal friction angle, φ_i (°)	27	25	19÷27
Dilation angle, ψ (°)	0	0	0
Tensile strength, σ_t (MPa)	7	3	0.1
Fracture energy release rate, G_f (J/m ²)	150	50	10
<i>Numerical parameters</i>			
Viscous damping (kg/ms)	5.00E+07	3.79E+07	3.79E+07
Normal contact penalty (GPa)	10	6	6
Tangential contact penalty (GPa)	1	6·10 ⁻¹	6·10 ⁻¹
Fracture penalty (GPa)	10	6	6

Table 7.14: Rock mass and shear zone mechanical properties used in the FDEM study.

<i>Trenches - Faults</i>	
Tensile strength σ_t (MPa)	0
Cohesion c (MPa)	0
Friction angle φ (°)	27

Table 7.15: Trenches and faults strength properties for FDEM models.

The numerical simulations were performed in two stages: 1) set the initial stress conditions, 2) simulate the instability of the slope. During both stages computation was led

to equilibrium. Figure 7.32 shows, for example, the decrease of the total kinetic energy during Stage 1 for the *circular surface* model; complete equilibrium is reached, with the number of cycles equal to $10 \cdot 10^6$ with a time step size of $1 \cdot 10^{-5}$, which correspond to a computation time of 17 days on a 2.33 GHz, 8 GB RAM pc. On the same computer, the Stage 2 required 12 days of computation.

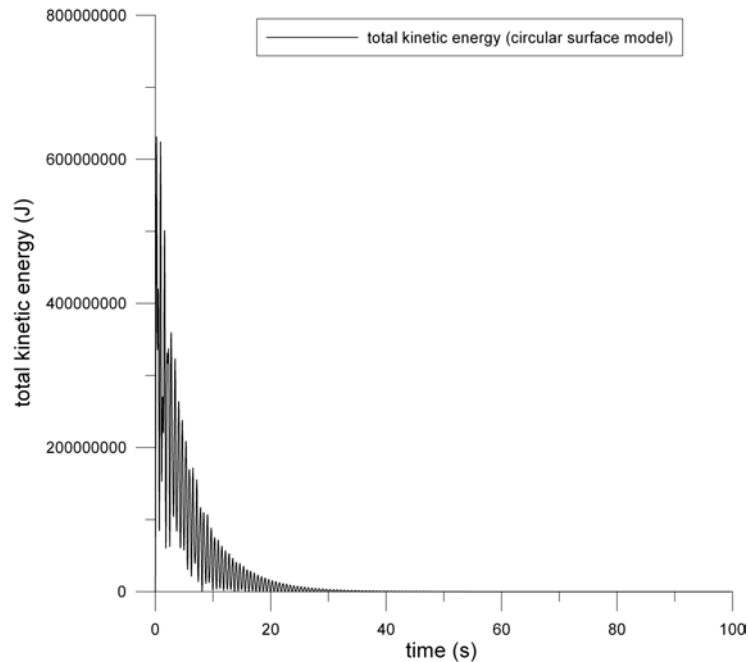


Figure 7.32: Total kinetic energy during Stage 1 of the FDEM simulation (*circular surface* model).

Figure 7.26 and 7.34 illustrate the FDEM simulation of instability. The mechanism driving instability is different in the two models. In the *rigid-block* model the shear zone attains failure, then the mass above starts sliding. As the movement increases, some tensile fractures develop inside the lower sliding body allowing the kinematic release. Further movement of the sliding mass causes the development of a heavily damaged portion of the slope between the upper stable zone and the sliding one, but the rupture does not develop in the upper part of the slope, and all the movement is confined downslope.

The kinematics observed in the *circular surface* model is quite different. The basal portion of the slope starts to slide above a circular surface composed by the one of the main scarp and the base shear zone. As the mass moves, several fractures develop inside such a portion of the slope. The movement of the lower portion causes the brittle fracture of the upper zone, where a new sliding surface develops. Such a model well represents the interaction between the lower portion of the Beauregard landslide, which it is observed to move above a shear surface completely developed (creep behaviour) and the upper portion of the slope which moves above an incipient sliding surface (brittle behaviour).

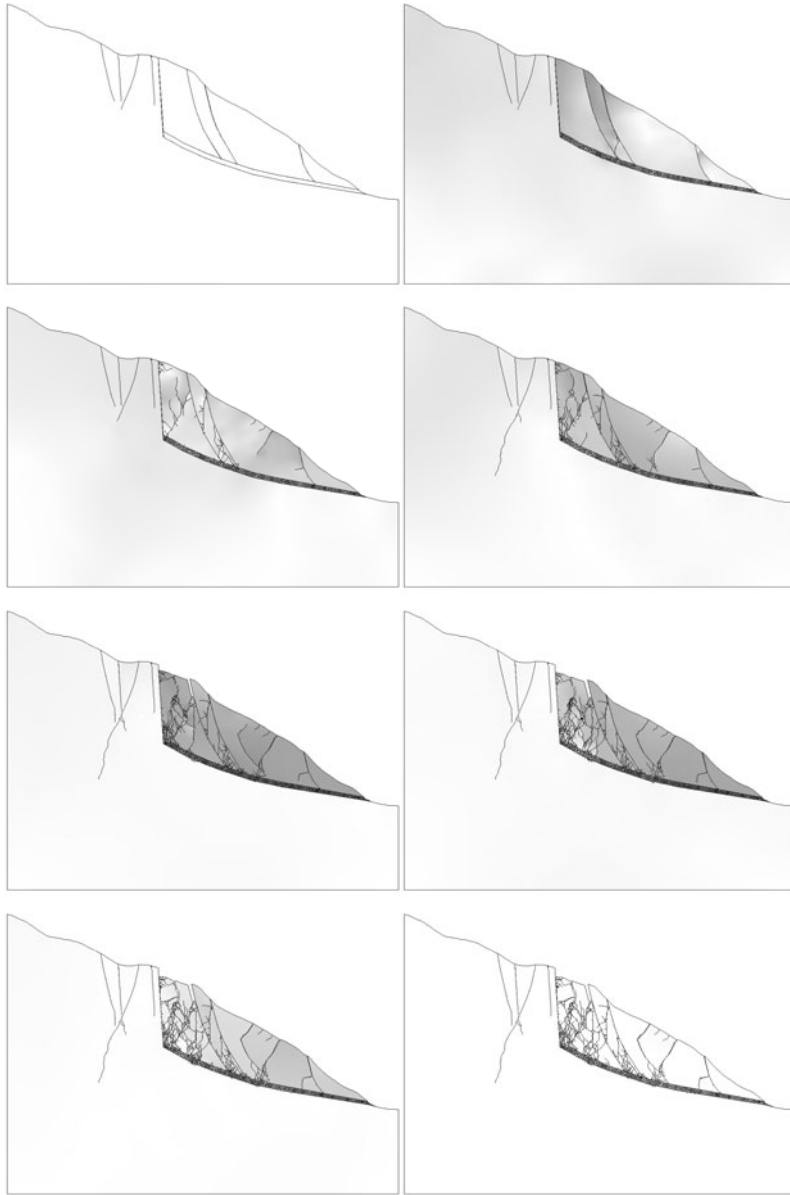


Figure 7.33: Subsequent screenshots of the instability simulated with Y2D code (*rigid-block model*) when the shear base has a friction angle of 19° .

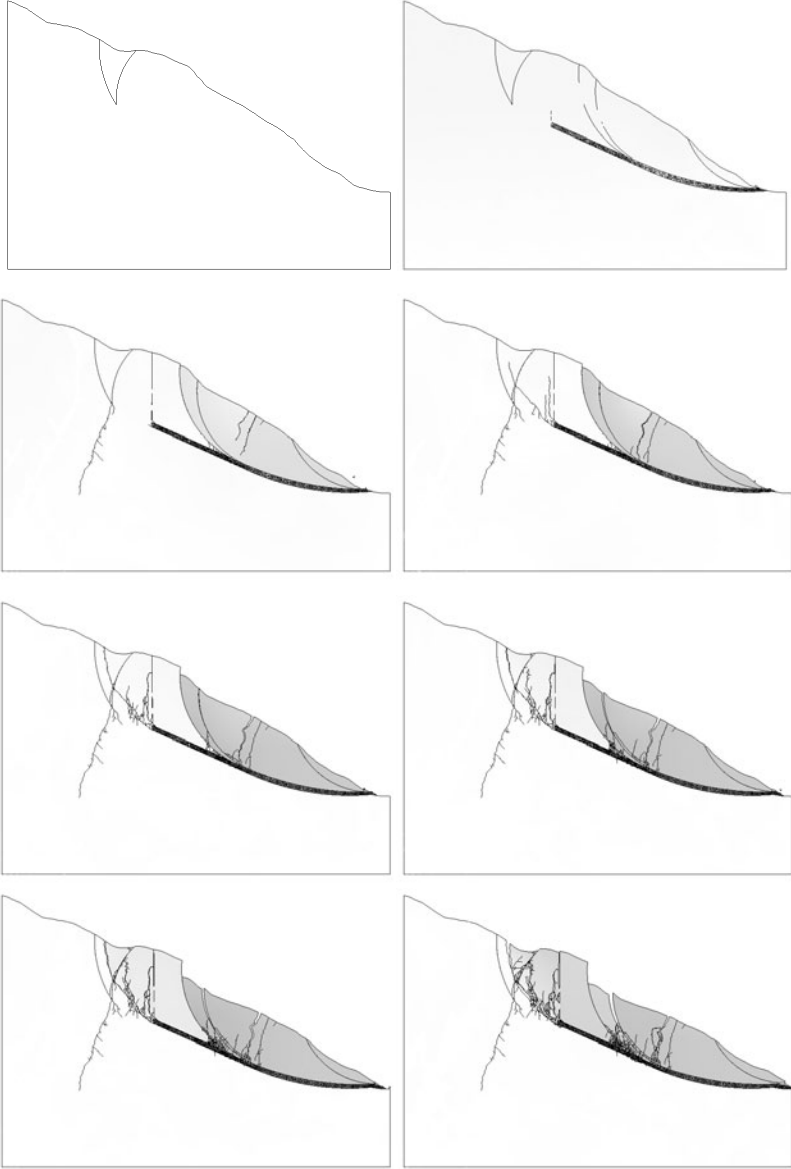


Figure 7.34: Subsequent screenshots of the instability simulated with Y2D code (*circular surface model*) when the shear base has a friction angle of 22°.

7.7 Summary

The results presented in this chapter analyse the characteristic modes of failure observed in the S-W portion of the Beauregard Landslide. Flexural toppling and local block toppling is highly dependent on discontinuity characteristics. Two main discontinuity sets which characterise the landslide influence the stability: the first one strikes parallel to the valley, the second one is perpendicular to it. Also the schistosity influences the development of instability.

In this study, discontinuity parameters including orientation and spacing were examined to evaluate the overall stability of the slope. Comparisons between FEM and FDEM analyses showed that the combined finite-discrete method allows to gain more information about triggering, subsequent evolution and deposition of the rock being mobilised in the failure process.

The characteristic failure mode of the Bochat area has been observed to be a sliding on a complex surface. The FDEM modelling study of such an area is able to describe this type of instability and the interaction between the lower portion of the slope and the upper part.

The combined finite-discrete element method is shown to account for the transition from continua to discontinua and represents a potential alternative to conventional analysis methods for slope stability analyses. A step forward in the application of such a technique to slope stability problems has been taken by showing its valuable help in the understanding of the modes of instability which characterise deep seated landslides from massive rock failure.

References

- Barla, G. (2009).** “Long-term behaviour of the Beaugard dam (Italy) and its interaction with a deep seated gravitational slope deformation. Invited Keynote Lecture.” In “5th Colloquium, Rock Mechanics - Theory and Practice,” Vienna University of Technology.
- Barla, G. (2010).** “Progress in the understanding of deep-seated landslides from massive rock slope failure.” In “ISRM International Symposium and 6th Asian Rock Mechanics Symposium New Delhi, India,” .
- Barla, G., Ballatore, S., Chiappone, A., Frigerio, A., and Mazzà, G. (2006).** “The Beaugard Dam (Italy) and the deep seated gravitational deformation on the left slope.” In “Hydropower 2006 - International Conference,” pages 99–112. Kunming, China.
- Hudson, J. A. and Harrison, J. P. (1997).** *Engineering Rock Mechanics. An Introduction to the Principles.* Elsevier Ltd.
- Kalenchuk, K., Hutchinson, D., Diederichs, M., Barla, G., Barla, M., and Piovano, G. (2010).** “Three-dimensional mixed continuum-discontinuum numerical simulation of the Beaugard Landslide.” In “European Rock Mechanics Symposium, Lausanne, Switzerland,” pages 639–642.
- Martinotti, M. (2010).** *Creep behaviour of cataclastic rock in massive rock slopes.* Ph.D. thesis, Politecnico di Torino, Dottorato di Ricerca in Ingegneria per la Gestione delle Acque e del Territorio.
- Miller, S., Barla, G., Piovano, G., and Barla, M. (2008).** “Geotechnical and temporal risk assessment of a large slope deformation.” In “42nd US Rock Mechanics Symposium and 2nd U.S.-Canada Rock Mechanics Symposium, San Francisco (USA),” .

Chapter 8

Summary and Conclusions

8.1 Summary

The following main tasks have been accomplished in the present thesis:

- a comprehensive review of the state-of-the-art on catastrophic massive landslides has been performed; each type of landslide from massive rock slope failure has been described: catastrophic rockslides; catastrophic spreads; rock avalanches; rockfalls; catastrophic debris flows; landslide from volcanoes; slow mountain slope deformations. Attention has been focused on deep-seated landslides; their origins and structural evolutions, together with morphological, geomechanical and structural features, have been pointed out. The occurrence of secondary types of movement in deep-seated gravitational slope deformations has been described;
- a review of numerical techniques used in rock slope stability analysis has been done, with emphasis on the use of combined continuum-discontinuum numerical modelling FDEM codes like a powerful tool to study the total slope failure of massive rock slopes;
- a description of the numerical formulation of continuum and discontinuum methods has been given; attention has been focused on the general formulation of the combined finite-discrete element method. The main algorithms which characterise this method have been discussed;
- a description of the Y2D code based on FDEM has been given; the Y-GUI and the Y2D input file data structure has been described. A series of numerical tests carried

out to provide a validation of the Y2D code has been presented. For each example, a description of the model set up and the relevant aspects which allow for reliable simulations have been given;

- a description of the geological and geomechanical conditions of the Beauregard Landslide, together with the interpretation of monitoring data has been reported; the main emphasis has been posed on the instability modes which characterise the landslide;
- the results obtained with FDEM numerical modelling of the main instability modes observed in the landslide have been described and discussed in detail.

8.2 Conclusions

Based on the research studies presented in this thesis, conclusions are drawn by covering the following main aspects:

- landslides from massive rock slope failure;
- numerical modelling of landslides from massive rock slope failure;
- combined Finite-Discrete Element Method;
- validation of the Y2D code by simulation of simple slope failure mechanisms;
- numerical modelling of key instabilities of the Beauregard massive landslide.

8.2.1 Landslides from massive rock slope failure

Hazard assessment of massive rock slope failure is made difficult by a variety of complex failure processes and unpredictable post-failure behaviour.

Deep-seated landslides are classified as a type of landslide from massive rock slope failure. Generally, there is yet some discussion on the understanding and description of such phenomena. Although these landslides have long been identified, their study has been restricted to the identification of morphological aspects and description of movement rates. Other types of slope instabilities are often linked with deep-seated gravitational slope deformations and have been recognised to have catastrophic consequences. There is agreement on the fact that the understanding of massive landslides and of the hazards connected with them requires a multidisciplinary approach using geological, geomorphological, geophysical and geotechnical studies, including monitoring methods for hazard management.

8.2.2 Numerical modelling of landslides from massive rock slope failure

The analysis of rock slope stability has changed significantly during recent years with a transition from limit equilibrium analyses to numerical modelling. These techniques have evolved to allow routine analysis treating the slope as either a continuum (e.g. finite-element method) or a discontinuum (e.g. discrete-element method). Furthermore, the complexity which characterizes most landslides from massive rock slope failure involves elements of both deformation of the continuum, interactions along existing discontinuities and the creation of new discontinuity features. To treat these problems, new developments in combined finite-discrete element codes have been proposed. These codes have demonstrated the significant potential in the analysis of “total slope failure processes”, from initiation through evolution and deposition.

8.2.3 The Combined Finite-Discrete Element Method

In the last decade of the 20th century, the Discrete Element Method has been coupled with the Finite Element Method. The new method is termed as “Combined Finite-Discrete Element Method” (FDEM) and was proposed by A. Munjiza. In the FDEM each body is represented by a single discrete element that interacts with the discrete elements close to it. Transition from continua to discontinua is done through fracture and fragmentation processes. The fractures modes considered are:

- Mode I - crack opening mode (a tensile stress normal to the plane of the crack is applied);
- Mode II - crack sliding mode (a shear stress acts parallel to the plane of the crack and perpendicular to it).

The fractures propagate at the boundaries of the discrete elements (i.e. the crack does not propagate inside the discrete element), once the fracture conditions in the material are reached. The FDEM has been implemented in a code named “Y code”. This code has been validated and used in this thesis in slope stability studies.

8.2.4 Validation of the Y2D code by simulating simple slope failure mechanisms

The use of the combined finite-discrete element method with fracture propagation capability enables the simulation of failure initiation and progressive development includ-

ing the fragmentation of the rock mass. In this thesis a number of complex slope instability mechanisms have been studied with the Y2D code.

The first series of models presented includes slopes characterised by the presence of pre-existing discrete discontinuity features; the purpose has been to simulate simple mechanisms of failure with the main purpose to gain in the understanding of the Y2D code when applied to the solution of slope stability problems. The generation of a failure surface was then analysed in a model which includes pre-existing sub-horizontal tectonic fractures with intact rock bridges. These fractures help to constrain the stepped development of the failure surface. The process of rock slope sliding along a stepped failure surface has been analysed in detail. Block toppling instabilities have been investigated to highlight the advantages of using FDEM when compared to analytical or DEM solutions. The assessment of the stability conditions for slope failure along a circular sliding surface through safety factors computation with FDEM is attempted and the results are compared with limit equilibrium and finite element method evaluations.

8.2.5 Numerical modelling of key instabilities of the Beauregard Landslide

The characteristic modes of failure observed in the S-W portion of the Beauregard Landslide have been analysed. Observed flexural toppling and local block toppling failures which are highly dependent on discontinuity characteristics have been simulated in detail with both FEM and FDEM models.

8.3 Recommendations and further developments

Further developments of the research work undertaken are needed. Future modelling work is envisaged toward the development of the code.

- To improve the applicability of the code to model large-scale landslides significant steps forward are needed toward the increase of computation speed. Actually the computation effort required by FDEM limits its applicability as tens of thousands of finite elements are essential for appropriate modelling.
- The presence of groundwater certainly affects the stability of a slope and appropriate numerical tools are yet to be developed and implemented in the FDEM code. New algorithms for hydro-mechanical coupling and fluid propagation inside newly created fractures is necessary.

-
- In order to improve the understanding of landslide mechanics 3D geometry has to be adopted in numerical modelling. The development of a 3D version of the code would allow for a more realistic representation of the landslide.

